Brno University of Technology
Student Branch

Proceedings of IEEE Student Branch Conference

Blansko 2018

10. - 11. 9.

Název: Proceedings of IEEE Student Branch Conference Blansko 2018

Editor: Miroslav Cupal

Vydavatel: Vysoké učení technické v Brně
Fakulta elektrotechniky a komunikačních technologií

Rok vydání: 2018

Vydání: první

Organizační výbor konference:

Ing. Miroslav Cupal
Ing. Martin Hrabina
Ing. Marek Novák

Tato publikace neprošla jazykovou úpravou.
Za obsah, původnost a literární citace odpovídají autoři jednotlivých příspěvků.

ISBN 978-80-214-5661-7

Conference was supported by

Gold sponsors

ROHDE & SCHWARZ

Silver sponsor

HTEST

Bronze sponsor

era

Other partners

IEEE Czechoslovakia Section

ÚREL ÚSTAV RADIOELEKTRONIKY

Preface

Dear friends,

it is already for the 14th time when you can read the Proceedings of a conference organized by IEEE Student Branch, Brno University of Technology. In its reborn tradition, we are happy to welcome you at the conference for recent and future PhD students.

The aim of the conference was always to bring together young scientist to share their ideas and to have the possibility of familiarizing with the research at other departments and universities and this year will not be an exception.

Organizing a conference is never an easy task. Therefore, we would like to thank all the companies and organizations that supported us, namely Rohde & Schwarz, HTEST and Era. Big thank you also belongs to IEEE Czechoslovakia Section and Department of Radio Electronics, Brno University of Technology.

To conclude, allow me to thank you, the participants of this year conference. By your participation, you support the very idea of what IEEE represents. We wish you a pleasant time in Blansko.

On behalf of the organizers

Miroslav Cupal

Table of content

Circularly polarized textile integrated antenna for ISM band 5.8 GHz

Miroslav Cupal
Department of radio electronic
Brno university of technology
Brno, Czech Republic
cupalm@phd.feec.vutbr.cz

***Abstract*—The paper presents textile integrated antenna used for integration into car or small airplanes for Wi-Fi connection. The antenna is based on substrate integrated technology. The antenna is designed for IMS band 5.8 GHz and it has directional radiation patterns and circular polarization.**

Keywords—textile antenna; 3D textile; substrate integrated; circular polarization; ISM band

I. Introduction

Textile integrated antennas are very popular in past years in field of wearable technologies as antennas for body-centric communication. The textile antennas are flexible and integrated to clothes or different materials. The antennas can be fabricated by conductive textile, conductive fibers or conductive screen printed technology.

Textile antennas can be integrated into airplane or bus upholstery and provide multimedia or internet for passengers and increase comfort of their journey. Because the concentration of passengers is relative height and data rate is bigger with 4K and 3D technology, it is suitable to use for example Wi-Fi standard IEEE 802.11a at frequency 5.8 GHz.

Several types of circularly polarized antennas on textile substrates have been published in past years in open literature. These antennas have been usually designed for ISM bands 2.4 GHz or 5.8 GHz [1]-[4]. These textile antennas have been conceived as linearly polarized and circularly polarized patch antennas [3], [5], printed dipoles [6], [7] or textile slot antennas [8].

The designed antenna is circularly polarized textile integrated slot antenna based on textile antenna presented in [9] and common antenna [10]. The design of textile integrated waveguide (TIW) and design of the antenna is described in Section 2 and simulations results given by 2 solvers are presented in Section 3.

II. Antenna Design

The antenna is designed on textile substrate call 3D textile (3D041) produced by Sintex company. The structure of the fabric is depicted in Fig. 1. The relative permittivity of the fabric is 1.2 [11] and the height equals to 3.4 mm and losses are given by tgδ = 0.002. Sidewalls are manufactured by silver conductive thread Elitex 440 dtex with conductivity 14 Ω/m and diameter 0.4 mm [12]. And top and bottom conductive layers are from self-adhesive copper foil.

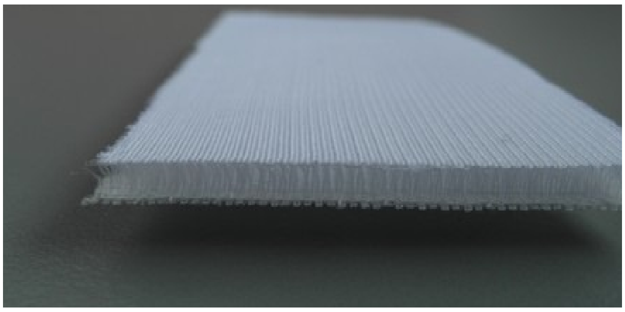

Fig. 1. The structure of 3D fabric 3D041.

The TIW technology is suitable according to height of the substrate and allows construct slot antennas and antenna arrays with relative good impedance bandwidth and radiation characteristics. The width of the TIW is given by equation (1) given by [13]:

$$w = w_{ef} + \frac{d^2}{0.95\,s}\,, \tag{1}$$

where w_{ef} is effective width of common rectangular waveguide, d is diameter of the thread and s is their spacing.

Because the sidewalls of the waveguide are approximated by metallic thread posts, the dense of the posts is given by formula (2) given by [13]:

$$\frac{s}{d} < 2\,, \tag{2}$$

where s is spacing between treads and d is diameter of the thread. Because the diameter of the conductive thread is 0.4 mm and antenna is hand made the distance between posts has been chosen to 1 mm.

The radiation element of the antenna is ring slot with cross slot inside (see Fig. 2). The position of the center of the ring slot is given by intensity of electromagnetic field inside TIW and is placed to maximum of intensity electric filed.

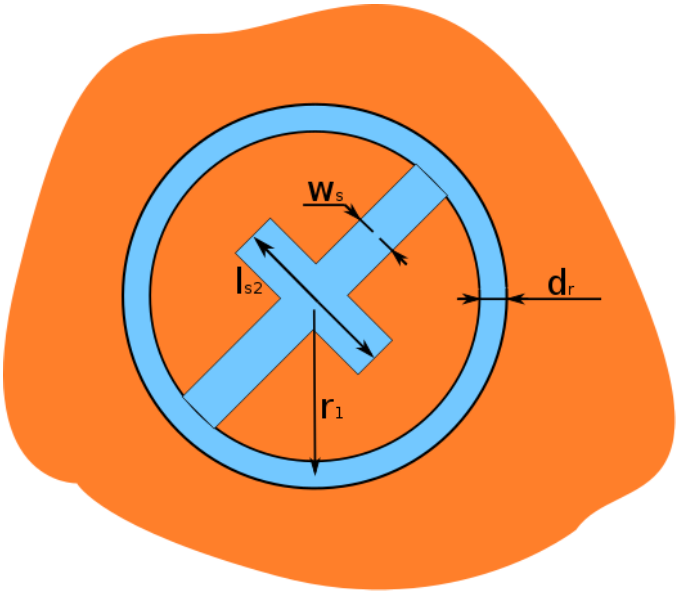

Fig. 2: Detail view of the radiation slot.

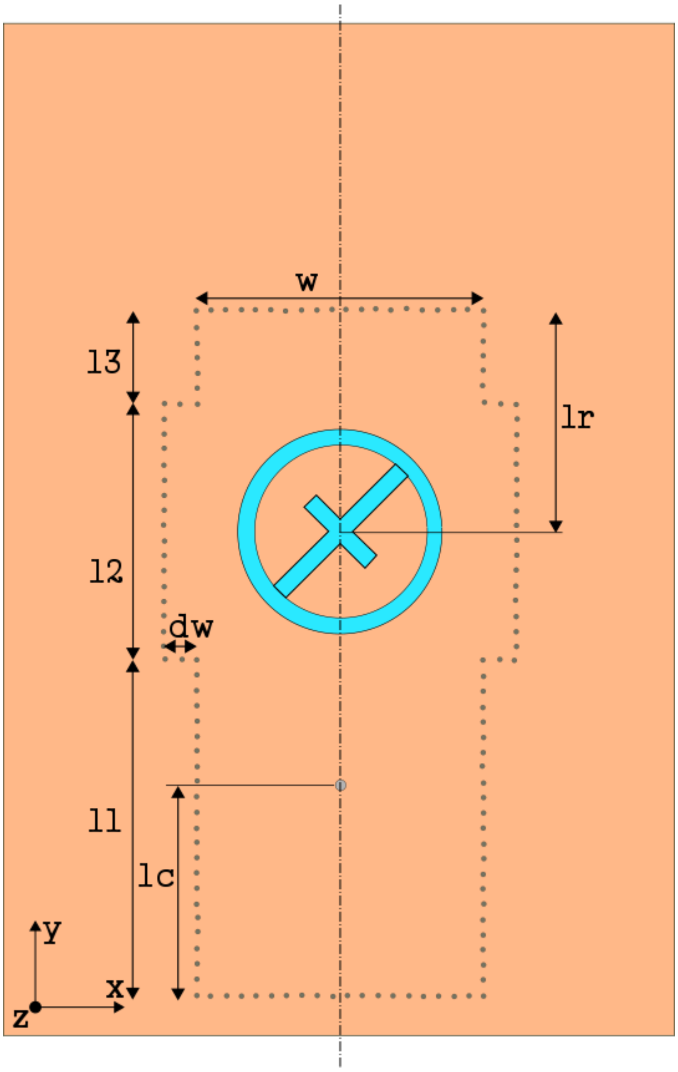

Fig. 3: The picture of the antenna with dimensions.

TABLE 1: ANTENNA DIMENSIONS.

w (mm)	l_1 (mm)	l_2 (mm)	l_3 (mm)	l_c (mm)	l_r (mm)
33.97	39.68	30.30	11.10	25.00	26.24
d_w (mm)	r_1 (mm)	l_{s2} (mm)	w_s (mm)	d_r (mm)	
3.90	11.21	10.04	2.04	2.04	

The middle radius of the ring slot is given by λ/4 and the width of the slot gives its impedance. The longest arm of cross slot is different than in [9]. The longest arm is connected to ring slot. This is given by different waveguide. Because in [9] dimensions according common rectangular waveguide, but now it is regular TIW. The length of the shortest arm of the slot is given by λ/4. The width of the both arms of cross slots according to width of the ring slot. All dimension of optimized antenna are depicted in Fig. 3 and 1.

The TIW is fed by common transition between SMA coaxial connector and substrate integrated waveguide. The center wire is connected to top metal layer of the TIW and shield is connected to the bottom layer and the center is placed to the λ/4 far from end of the waveguide.

III. SIMULATION RESULTS

The antenna has been simulated in CST Microwave Studio. The conductive walls have been simulated as metal columns connected to the top and bottom metal layers. The textile material has been simulated as substrate with relative permittivity 1.2 and tg δ 0.002.

The simulations have been performed by two different solvers. The first solver is Time domain solver based on Finite Integration Technique (FIT) and the second solver is Frequency solver based on the Finite Element Method (FEM). Results of booth solvers are compared.

Because both solvers use different mesh, it is good to describe settings of meshes. The Time solver uses hexahedral mesh and the setting was:

- mesh-cells:1863680
- cells per wavelength: 22
- cells per max model box edge: 12 (6 far from model)

Simulation accuracy has been set to -40 dB and time step 2,295e-4 ns. The Frequency solver use tetrahedral mesh with follows parameter:

- mesh-cells: 924994
- cells per wavelength: Automatic
- cells per max model box edge: 12 (1 far from model)

and solver type Iterative and adaptive mesh refinement was activated (phases **3**-8).

The simulated frequency responses of reflection coefficient are in Fig. 4. The impedance bandwidth for S_{11}<-10 dB of the antenna covers all ISM band 5.8 GHz and it is 350 MHz (time solver) and 382 MHz (frequency solver). The difference of both solver is 32 MHz. Next important parameter is axial ratio bandwidth for AR<3 dB. The AR bandwidth for time solver is 185.3 MHz and for frequency solver 192.8 MHz, but it is shifted to higher center frequency 5.90 GHz. There is a relative big difference between both solvers. The frequency responses of AR are in Fig. 5.

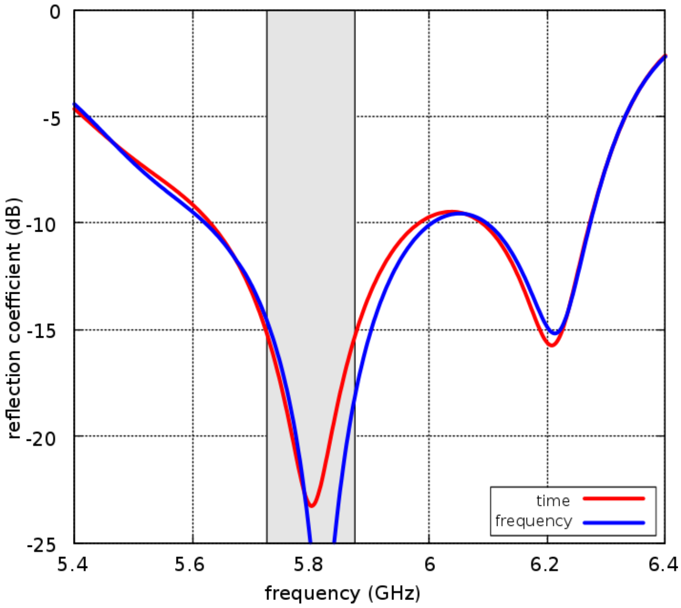

Fig. 4: Frequency response of the reflection coefficient.

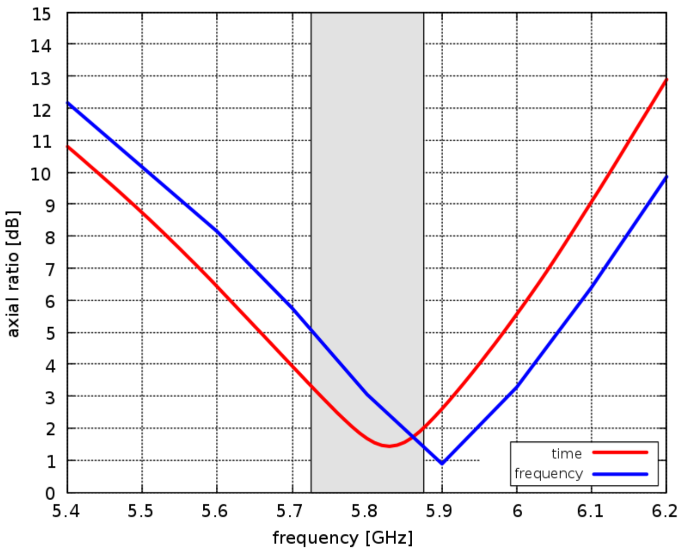

Fig. 5: Frequency response of axial ratio for direction perpendicular to the antenna.

The radiation patterns in Cartesian view are in Fig. 6 and Fig. 7. The patterns for plane XZ are in Fig. 6 and the maximal gain of the antenna is 6.51 dBi (given by time solver) and 6.96 dBi (given by frequency solver). The antenna radiation patterns has path antenna shape and radiates perpendicularly to antenna plane. The main lobe width is 96.1° in plane XZ and 95.4° in plane YZ. The back lobe level is suppressed by 18.02 dB.

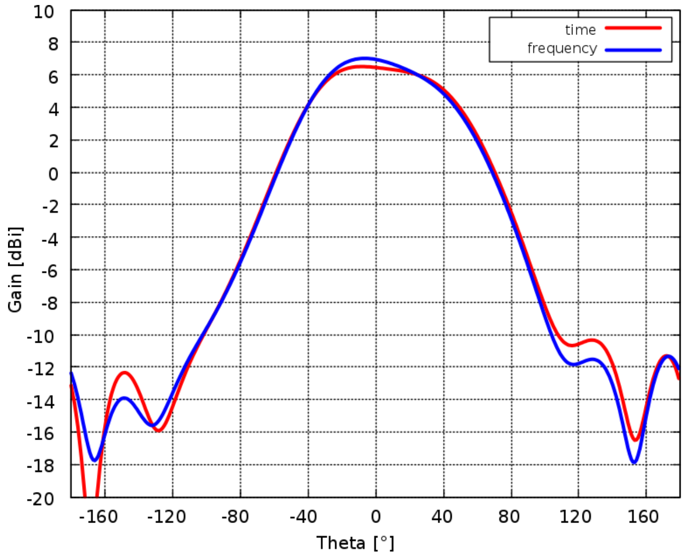

Fig. 6: Radiation patterns in Cartesian view for plane XZ.

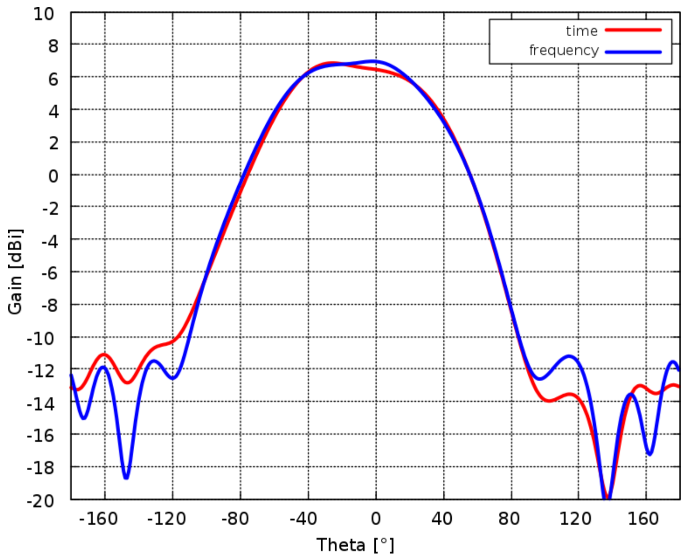

Fig. 7: Radiation patterns in Cartesian view for plane YZ.

IV. Conclusion

The circularly polarized ring slot antenna completed by the cross-slot was presented in the paper. The antenna was designed for ISM band 5.8 GHz to be integrated into textile upholstery of airplanes. The antenna was simulated into two solvers and results ware compared. At the frequency 5.8 GHz, the gain of the antenna was 6.51 dBi, and the axial ratio bandwidth is 185.3 MHz for |AR|<3 dB. The biggest difference is in Axial Ratio minimum, where frequency solver shifts the minimum to frequency 5.9 GHz.

Acknowledgments

The research was supported by the MPO TRIO project FV10087. For simulations and experiments, equipment of the SIX Center was used (the grant

LO1401). A partial support of Brno University of Technology is acknowledged (the grant FEKT-S-17-4713).

References

[1] M. Rizwan, Y. Rahmat-Samii and L. Ukkonen, "Circularly polarized textile antenna for 2.45 GHz," 15 IEEE MTT-S 2015 International Microwave Workshop Series on RF and Wireless Technologies for Biomedical and Healthcare Applications, Taipei, 2015, pp. 21-22.

[2] S. K. Mishra, V. Mishra and N. Purohit, "Design of wide band circularly polarized textile antenna for ISM bands at 2.4 and 5.8 GHz," 2015 IEEE International Conference on Signal Processing, Informatics, Communication and Energy Systems (SPICES), Kozhikode, 2015, pp. 1-5.

[3] M. Klemm, I. Locher and G. Troster, "A novel circularly polarized textile antenna for wearable applications," 7th European Conference on Wireless Technology, 2004, Amsterdam, The Netherlands, 2004, pp. 285-288.

[4] E. K. Kaivanto, M. Berg, E. Salonen and P. de Maagt, "Wearable Circularly Polarized Antenna for Personal Satellite Communication and Navigation," IEEE Transactions on Antennas and Propagation, vol. 59, no. 12, pp. 4490-4496.

[5] M. Tanaka and Jae-Hyeuk Jang, "Wearable microstrip antenna," IEEE Antennas and Propagation Society International Symposium. Digest. Held in conjunction with: USNC/CNC/URSI North American Radio Sci. Meeting (Cat. No.03CH37450), Columbus, OH, USA, 2003, pp. 704-707 vol.2.

[6] L. Ukkonen, L. Sydanheimo, and Y. RahmatSamii, “Sewed textile RFID tag and sensor antennas for on-body use,” 6th European Conf. Antennas and Propagation (EUCAP), pp. 3450 – 3454, Mar. 2012.

[7] T. Kaufmann, I.-M. Fumeaux, and C. Fumeaux, “Comparison of fabric and embroidered dipole antennas,” Proc. 7th EuCAP, Gothenburg, Sweden, Apr. 2013.

[8] R. Moro, S. Agneessens, H. Rogier and M. Bozzi, "Wearable textile antenna in substrate integrated waveguide technology," in Electronics Letters, vol. 48, no. 16, pp. 985-987, August 2 2012.

[9] M. Cupal and Z. Raida, "Circularly polarized substrate integrated textile antenna for ISM band 24 GHz," *2017 International Conference on Electromagnetics in Advanced Applications (ICEAA)*, Verona, 2017, pp. 1154-1157

[10] H. Iwasaki, "A circularly polarized small-size microstrip antenna with a cross slot," in *IEEE Transactions on Antennas and Propagation*, vol. 44, no. 10, pp. 1399-1401, Oct. 1996.

[11] J. Špůrek, J. Vélim, M. Cupal, Z. Raida, J. Prasek, and J. Hubalek, “Slot loop antennas printed on 3D textile substrate,” in Proc. MIKON, Krakow, Poland, 2016.

[12] CUPAL, M. Conductive Threads for Microwave Applications. In Proceedings of IEEE Student Branch Conference Mikulov 2017. Brno: VUT v Brně, 2017. p. 15-17. ISBN: 9788021455269.

[13] M. Bozzi, A. Georgiadis and K. Wu, "Review of substrate-integrated waveguide circuits and antennas," in *IET Microwaves, Antennas & Propagation*, vol. 5, no. 8, pp. 909-920, 6 June 2011.

Near-Field Time Domain Chipless-RFID System with Sequential Bit Reading

Jaroslav Havlíček
Department of Electromagnetic field
Czech Technical University in Prague
Prague, Czech Republic
havlij18@fel.cvut.cz

***Abstract*—This paper presents chipless RFID near field system with sequential bit reading based on time domain information coding. Key part of the reader is an open stub connected to a microstrip line. The stub can be described as band stop filter. The tag is composed of strip resonators with same length (half-wavelength dipoles). Coupling between the stub and the strip resonator causes a significant variation of transmission coefficient at resonant frequency of the stub. This variation can be used for information (bit) coding. The first designed system is working at the first resonance of the stub (length 90 degrees). The second system is working at the second resonance of the stub (length 270 degrees) and it was designed in order to increase tag per unit length bit capacity. Performance of both first and second resonance systems were verified by measurement by 40-bit tag with bit capacity 5 bit/cm and 100 bit tag with capacity 16.7 bit/cm respectively.**

Keywords*—*chipless RFID, tag, half-wavelength resonator, microstrip

I. Introduction

The radiofrequency identification (RFID) is a widespread technology, which is applied mainly in industry (production process monitoring), logistics (acceleration of storing procedures), commerce (antitheft feature), health care (elimination of patient confusions) and inventorying (e.g. books in libraries). RFID is expected to have an important role in the internet of things concept [1].

There is a perfect opportunity for further spreading in commerce, provided that the RFID transponders (tags) are suitable for optical barcode replacement [2]. The advantage of the tag consists in the possibility to be read without necessity of clear line of sight. Low price of the tag is essential for reaching this goal. Unfortunately conventional tags which consists a chip are about hundred times more expensive than barcode [3]. Perspective approach to reduce the tag cost is chipless RFID which provides different methods of storing information without chip.

Promising examples of the chipless RFID technology are tags based on spectral frequency domain [4-7], and also some tags working in time domain [8-9]. Both these groups of tags in most cases consist of resonating scatterers. Presence or non-presence of each scatterer (resonator) represents logic one or zero, respectively. This logic information can be coded either into tag spectral signature (frequency domain tags) or tag time response.

II. System Principle

System presented in this paper is based on time domain bit coding with sequential bit reading in near field. Tag composed of strips (half-wavelength dipoles) is moving above the stub of the reader, see Fig. 1. The stub end is open. Resonant frequency of the stub, where is minimum transmission coefficient $|S_{21}|$ of the reader, is used as a reading frequency f_0.When the stub and a strip are perfectly aligned with each other $|S_{21}|$ at f_0 rises close to 0 dB. This significant change of transmission coefficient is used for information coding. Logic zero is coded by detuning (cutting) the strip, see Fig. 2. System based on same principle has been already presented [9].

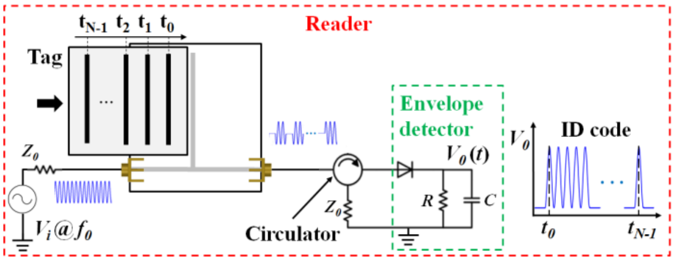

Fig. 1. Working principle of the time domain chipless RFID system

There are two versions of the system, first is using first resonance frequency of the stub (stub electrical length is 90 degrees) as f_0 and second system second resonance frequency (270 degrees). Performance of both systems were verified by measurement, 40-bit tag with bit density 5 bit/cm in case of first resonance system and 100 bit tag with bit density 16.7 bit/cm in case of second resonance system.

III. Topology

For both versions of the system the active part of the reader (stub-loaded line) was designed in microstrip technology by loading a 50 Ω line. The considered substrate is *Rogers RO3010* with dielectric constant ε_r = 10.2 and thickness h = 0.64 mm. The width of the 50 Ω line is 0.6 mm. The layout of the active part of the reader is shown in Fig. 2a. The half-wavelength resonators of the tag was designed on the *Rogers RO4003C* substrate with dielectric constant ε_r = 3.55 and thickness h = 0.2 mm. Width of each tag resonant strip is 0.4 mm for both versions, in order to maximize the per unit length information capacity of the tag (where the resonant elements are disposed orthogonal to the tag chain axis).

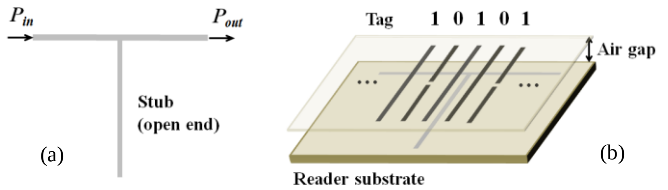

Fig. 2. Layout of the active part of the reader (a). Reader and fragment of the tag (b) with an example of coding '0' by detuning a strip (cut in the middle)

In the first version the length of the open stub is 8 mm (electrical length 90 degrees) and its width is 0.4 mm. The length of the each tag strip is 30 mm. Separation between them is 1.6 mm and their period is 2 mm which provides bit capacity 5 bit/cm. The tag contains 40 strips (40 bits).

In the second version the length of the open stub is 26 mm (electrical length 270 degrees) and its width is 0.2 mm. The length of the each tag strip is 34 mm. Separation between them is 0.2 mm and their period is 0.6 mm which provides bit capacity 16.7 bit/cm. The tag contains 100 strips (100 bits).

IV. SILULATION RESULTS

Simulation results in the case of first version system are depicted in Fig. 3. When there is only one strip aligned above the stub (blue line), there are two resonant dips instead of one when there is only reader without the tag (black line). Same effect can be explained using coupled resonant circuits theory. Rest of $|S_{21}|$ lines in Fig. 3 is showing effects of different 5-bit words. Middle strip (bit) is read in all these cases (red and magenta is '1', green and cyan is '0'). Multiple coupling between tag strips causes parasitic dips which are dependent on particular bit word. Considering this was reading frequency f_{01} set to 3.64 GHz which provides slightly less $|S_{21}|$ than frequency of the single strip peak (blue line).

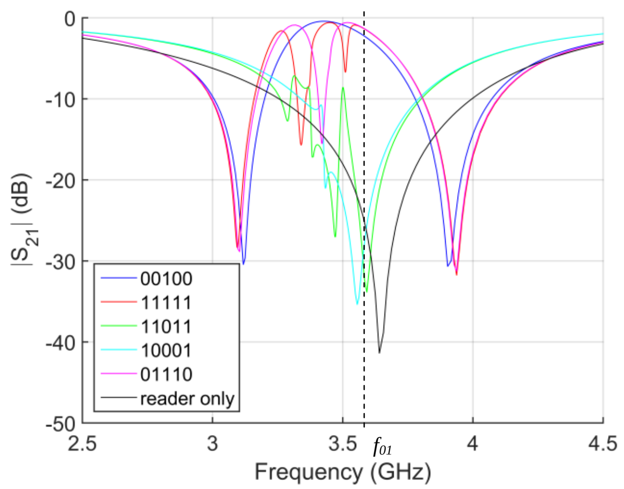

Fig. 3. First version of the system, frequency response for different bit words

Frequency position of all resonant dips is also dependent on air gap width between tag and reader substrates which have an influence on effective dielectric constant of the whole system. From this point of view is not very convenient to use for bit reading a frequency of a peak which has a high slope as a consequence neighboring parasitic dip. Frequency distance between the dip minimum and f_{01} is only circa 100 MHz.

Second version was designed in order to solve this problem. Parasitic dips are in this case completely out of the stub second resonance dip band, see Fig. 4 (black line). Reading frequency f_{02} = 3.47 GHz was set as a compromise between bit word containing a single '0' and word with couple of '0' in row (green and cyan line respectively). Absence of parasitic dips proximity to f_{02} provides more than 3 times higher per unit length bit capacity with slightly better dynamic range and comparable robustness against reader to tag air gap width fluctuation.

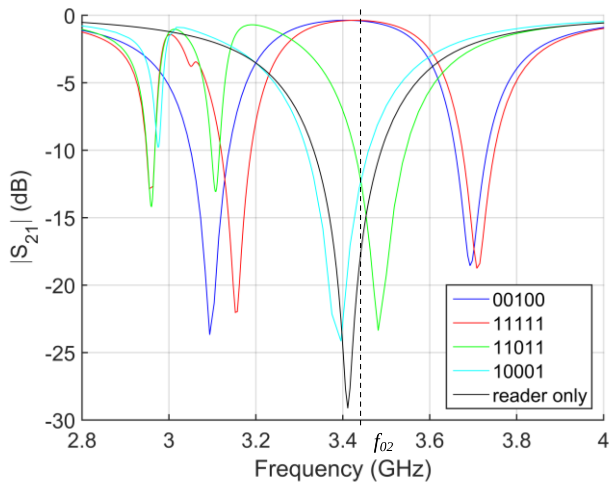

Fig. 4. Second version of the system, freq. response for different bit words

V. MEASUREMENT

Both versions of proposed system were experimentally validated. Tags were fabricated using standard photo-etching, with all strips intact (all bits set to '1'). Coding '0' by cutting (detuning) desired strips in their middle was done later manually. The reader was fabricated by means of a *LPKF HF-100* drilling machine (the photographs of second version are depicted in Fig. 5). Measurements were conduct using the same set-up as presented in [8], consisting of a function generator, an envelope detector and an oscilloscope (to display the time domain response of the tag, i.e., the AM signal containing the ID code), plus the mechanical guiding system, see Fig. 1.

The measured envelope is depicted in Fig. 6 and Fig. 7 for the first and the second version respectively. The measured normalized envelope reveals the presence of logic '0' states (as dips in the time-domain responses). Thus, tag programming can be simply done by cutting the required resonant elements, similar to [8], [9]. All bits in both versions can be easily recognised although neighbouring logic '1' in second version are separated by only insignificant dips. If reader decoding system need deeper dips it can be achieved by larger separation of strips at the cost of lower per unit length bit capacity.

(a)

(b)

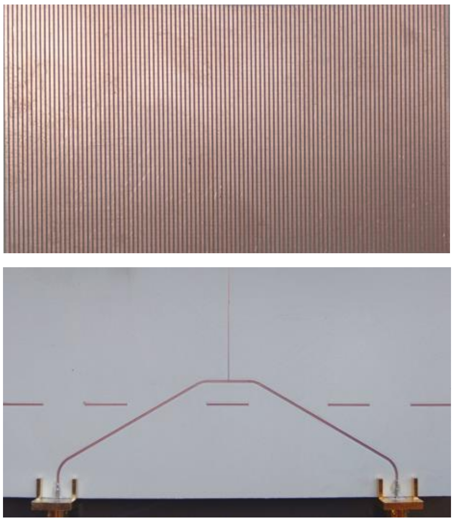

Fig. 5. Fabricated second variant system, 100-bit tag with all bits set to the logic '1' (a), and reader (b). Size of the tag is 60 mm × 34 mm.

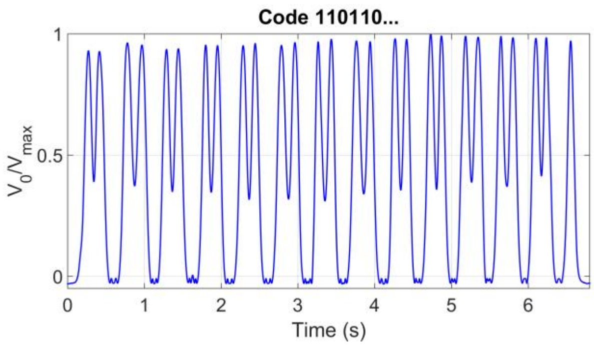

Fig. 6. Measured normalized envelope of the first version tag (40-bit)

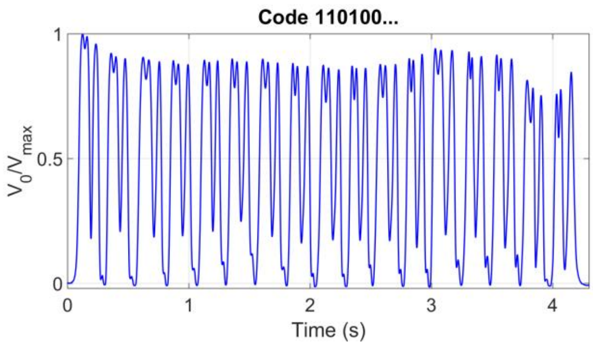

Fig. 7. Measured normalized envelope of the second version tag (100-bit)

VI. CONCLUSION

The paper discusses design and performance of chipless RFID near field system with sequential bit reading based on time domain information coding, where the reader is composed of microstrip line with open end stub and the tag is composed of chain of strips which can be described as half-wavelength dipoles. First version of the system is using first resonance of the reader stub and achieved bit capacity 5 bit/cm in 40 bit tag. Due to parasitic coupling between tag strips was this solution potentially vulnerable to reader to tag air gap width fluctuation which decreases reading robustness. Second version of the system is using second resonance of the reader stub solved the parasitic coupling problem and thanks to it achieved significantly higher bit capacity 16.7 bit/cm in 100 bit tag.

ACKNOWLEDGMENT

This work was supported by the Czech Technical University in Prague under the project SGS16/226/OHK3/3T/13.

REFERENCES

[1] S. Dey, J. K. Saha and N. C. Karmakar, N. Smart Sensing: Chipless RFID Solutions for the Internet of Everything. IEEE Microwave Magazine, 2015, vol.16, no.10, pp.26-39. DOI: 10.1109/MMM.2015.2465711

[2] P. Harrop, R.Das, *Printed and Chipless RFID Forecasts, Technologies & Players 2011-2021.* [Online] Cited 2016-04-25. Available at: http://www.idtechex.com/research/reports/printed-and-chipless-rfid-forecasts-technologies-and-players-2011-2021-000254.asp.

[3] S. Preradovic, and N.C. Karmakar, "Chipless RFID: Bar Code of the Future," *IEEE Microw. Mag.*, vol. 11, no. 7, pp. 87-97, Dec. 2010.

[4] R. Rezaiesarlak, and M. Manteghi, "Complex-Natural-Resonance-Based Design of Chipless RFID Tag for High-Density Data", *IEEE Transactions on Antennas and Propagation*, vol. 62, no. 2, pp. 898-904, 2014.

[5] A. Vena, E. Perret, and S. Tedjini, "A Fully Printable Chipless RFID Tag With Detuning Correction Technique", *IEEE Microwave and Wireless Component Letters.*, vol. 22, no. 4, pp. 219-229, 2016.

[6] J. Havlicek, M. Svanda, J. Machac, M. Polivka, "Improvement of Reading Performance of Frequency-Domain Chipless RFID Transponders", Radioengineering, vol. 25, no. 2, pp. 209-211, 2012.

[7] M. Polivka, M. Svanda, J. Machac, Chipless RFID Tag with an Improved RCS Response, *Proc. of 44th European Microw. Conf.* (EuMC), 2014, pp.770-773, ISBN: 9781479955985, DOI: 10.1109/EuMC.2014.6986548

[8] C. Herrojo, J. Mata-Contreras, A. Núñez, F. Paredes, E. Ramón, and F. Martín, "Near-field chipless-RFID system with high data capacity for security and authentication applications", *IEEE Trans. Microw. Theory Techn.*, vol. 65, no. 12, pp. 5298-5308, Dec. 2017.

[9] C. Herrojo, J. Mata-Contreras, F. Paredes, A. Núñez, E. Ramon, and F. Martín, "Near-field chipless-RFID system with erasable/programable 40-bit tags inkjet printed on paper substrates", *IEEE Microw. Wireless Compon. Lett.*, vol. 28, pp. 272-274, Mar. 2018.

Current Sharing in paralleled Six Phase Step-Up DC-DC converter

Erik Herceg
Department of Radio electronic
Brno university of technology
Brno, Czech Republic
herceg@feec.vutbr.cz

***Abstract*— This article is dealing with paralleled three DC-DC converters in 6-phase operation. Paralleling commercially available DC-DC convertors to achieve high current capability can be a challenging task. The main problem is the way how the sensing of output current is solved and thus the current sharing may be problem. Using series diode at the output, or finding correct load sharing circuit may help, but functionality of load sharing circuits can be used only with certain convertors. Main function of these three paralleled current controllers is to boost 24 V at the input to 28 V at the output with current capability up to 100 A. The aim of this document is to give an idea of a simpler way for parallelism of converters, to stress the importance of length matching, minimization of the high frequency spikes and to discover advantages of multiphase operation.**

(*Abstract*)

Keywords—DC-DC convertor, Step-Up, Boost converter, paralleled convertors, sychronization, current sharing error, length matching, half-bridge

I. INTRODUCTION

As known switching convertors are used almost in every electronic device. These types of convertors have many advantages, but on the other hand sometimes they cannot be used in every application, because of its undesired parameters. The key advantage is the high efficiency, which can be achieved up to 97% so the power dissipation is small and therefore no heat sink is needed. Design of high current DC-DC boost converters requires high capacity at the output for achieving lowest voltage ripple. Minimum voltage ripple can be achieved by increasing the switching frequency and the output capacitance can be smaller, but for example in RF devices these higher frequencies together with high frequency spikes can cause problems due to higher harmonics of switching frequency, which can occur at the output voltage. To minimize the voltage ripple in low power devices can be performed by using the low-dropout regulator, but this method is not possible to apply on the application described in this project. High frequency noises created by switching of MOSFET's can be minimized by adding low-pass LC filter. These are the main parameters which must be maximally eliminated, when convertor has to pass through EMC and EMI tests.

There are many types of switching convertors, we can divide them into two main groups according to voltage transformation (Buck / Boost / Buck - Boost) and isolation (Isolated / Non-Isolated). When higher current capability of converter is needed, the best way is to build a custom convertor, but this solution is time consuming. One of option is to parallelization of convertors.

Load sharing or load balancing techniques are important when the current distribution has to be equaled to all paralleled DC-DC convertors. It is also important how these convertors are connected. Ideally all traces or cables to load should be length matched or when this is not possible, the current compensation loop should be corrected to equalize the shared current. The main aim is to make the same condition for all converters.

In this project three current controllers are paralleled, each of them has its own current compensation loop and all of them have one common voltage loop. Used outer voltage loop is the boost mode compensation type II [1] which is simple comparator, where the is output voltage connected through resistor divider to operational amplifier and it is compared with reference voltage. The N-channel MOSFET's are connected in half bridge. High and low side consist of two parallel MOSFET switches, which is capable to deliver 420 W of power. Each driver has two channels, which works separately, and its phase is shifted by 120°. When three drivers are connected, there are two options of multiphase operation, first is 120° and second 60° operation. Sixty degrees operation needs and external source of synchronization signal, which generates two synchronization signals, first with 0°-degree phase shift and second with 180° phase shift so the MCU is necessary.

Current controller has an internal oscillator, which determines switching frequency. When synchronization signal from another current controller is connected to a driver, an internal oscillator is overdriven by this external signal. Frequency is set by external resistor and in this project was set to 150 kHz. Every controller has synchronization input and output pin, which generates low duty cycle PWM and can set the oscillation frequency to other controller.

Many articles were published, where load sharing techniques were described. The most challenging is to minimize error of load sharing between individual channels. With series diode connected after each convertor, there are no available data, which proves error in current share. In more complex paralleled converters these simple series diode isolators were replaced with "lossless" OR-ING controllers [6], which isolates common output line with individual outputs of controllers. OR-ING controller is always controlling the MOSFET transistor, which can be used for low or high side of convertor. Load sharing circuits represent another step further as these are able to minimize current sharing error under 5 % [5] Driver used in this project can theoretically achieve under 1 % of current accuracy [2]. The accuracy achieved in this project was less than 0.5 % under full load. Problematics with power sharing circuits and its study in consideration with frequency, output impedance and dynamic response was described in [3].

II. Concept of DC-DC Convertor

A. Main Topology

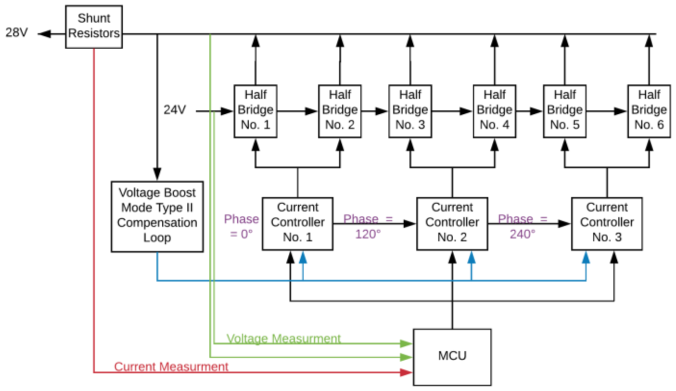

Fig. 1. Topology of parallelized DC-DC convertor

Topology of parallelized three DC-DC step up convertors is shown at Fig. 1. Convertor can measure all main parameters as output and input voltage, output current. Input current is measured at every controller separately, so the current share can be compared. The temperature is measured through MCU at every high side part of half bridge by temperature sensors, so when the maximum temperature is reached the controllers are turned off to protect transistors of overheating and following destruction of transistor. The current share error between individual current controllers is shown on Fig. 4.

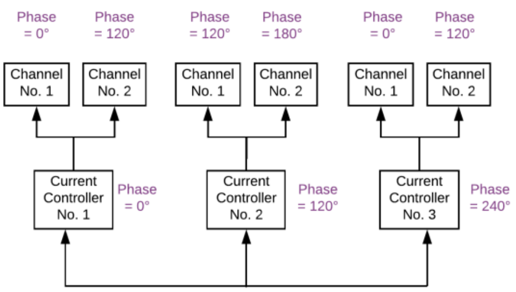

Fig. 2 Phase shift of each controller and its two channels

At Fig. 2. is demonstrated how is the phase shifting of each current controller. Every controller is able to drive two channels of half bridges. Phase shift between these two channels is equal to 120°. Three controllers have 120° phase shift between themselves, so this whole controller works in six phase operation, what means that overall phase shift between all half bridges is 120°. The synchronization input and output signals are displayed at Fig. 3. These synchronization signals were captured with logic analyzer. Due to these phase shifts the switching is not at the same time what prevents sum of the switching voltage spikes at rising or falling edge of driving signals.

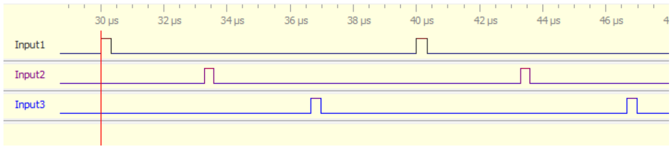

Fig. 3. Synchronization pulses

III. Problematics of Parallization

A. Current Sharing error between particular convertors

The reduction of current sharing error is the most important part in parallelization of convertors. This value is calculated as difference of current between all channels with regard to total current. This is important for achievement of current, temperature and power dissipation equality. As can be seen on Fig. 4. the current sharing error is decreasing with higher output current. DC resistance of trace from convertor to load has significant impact on current sharing error. Every convertor's current loop is compensated due to different distance of each convertor to load. The main parameter, which is different for each convertor is DC resistance of trace from output of convertor to output connector which is influencing the current loop. Total current sharing error of each convertor achieved 0.15 % when output current was 80 A. Final values of each controller were: 30.78 A for CC1, 30.718 A for CC2 and 30.77 A for third current controller.

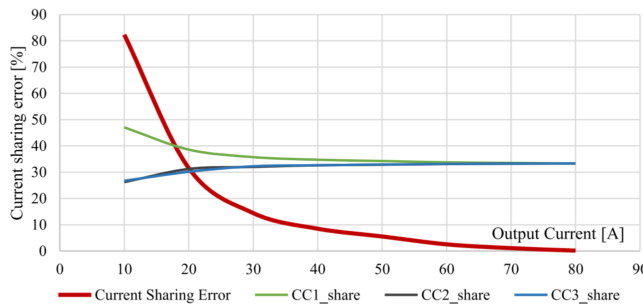

Fig. 4. Current sharing error in compare to output current

$$CS_{error} = 100 \times \frac{I_1 - I_2 - I_3}{(I_1 - I_2 - I_3)/3}\ [\%] \tag{1}$$

The total current sharing error was calculated with equation 1. where at nominator are all three currents subtracted and in denominator, all currents are summed and divided by total number of currents. This value is multiplied by 100 to get result in percentage. This equation can be used for any number of paralleled controllers with minor adjustment.

B. *Current Sharing error between particular channels*

Apart of comparing current sharing error between individual controllers, it should be also focused on current sharing between particular channels of each controller. On figure 4. the fault at current sharing in the first current controller can be spotted, which has major impact on total current sharing error. This incorrect current sharing is decreased with higher output current, so when the converter was full loaded the error was decreased under 1 %. The current share of other two controllers was almost the same.

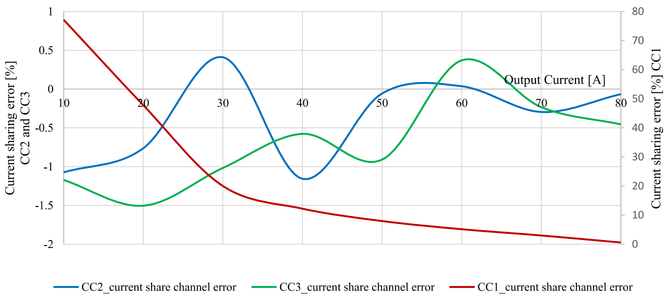

Fig. 5. Current sharing error between individual channels

C. *Length matching from drivers to transistors*

Error of current share is influenced by length match of high and low side gate drivers. The length of the gate driver signals must be the same for both channels and for all converters. Difference of wrong current sharing can be noticed in two paralleled transistors. Transistor connected closer to gate driver conducts more current than second transistor. This was noticed by temperature measurement, when the converter was delivering 80 A at the output. The temperature of second transistor was about 5° degrees below towards to first transistor. At Fig.6. the wrong and right way of traces to gates of paralleled transistors is shown. On the left picture length of trace is different for both transistors and the right picture shows the right way how to connect traces to transistors, where the length is matched. Traces are highlighted by purple color.

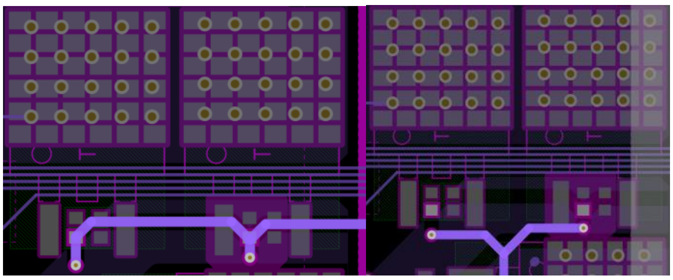

Fig. 6. Wrong gate trace to paralleled transistors (left picture) and correct trace to transistor gates (right picture)

IV. FINAL MEASURED RESULTS

Exact frequency was set 150 kHz and duty cycle of high side switch was 77 %. In Fig. 7. are shown curves of high and low side drivers. The voltage reached by voltage spikes were almost 44 V. These high frequency spikes can be seen on Fig. 8. where is output voltage after low pass LC filter at the output. Cut-off frequency of output low pass filter was 14.147 kHz and the magnitude in bode diagram at 150 kHz was -37 dB.

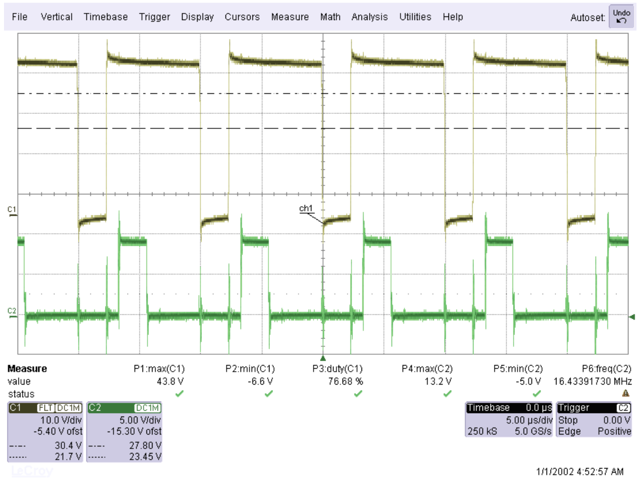

Fig. 7. Picture of PWM at high and low side drivers.

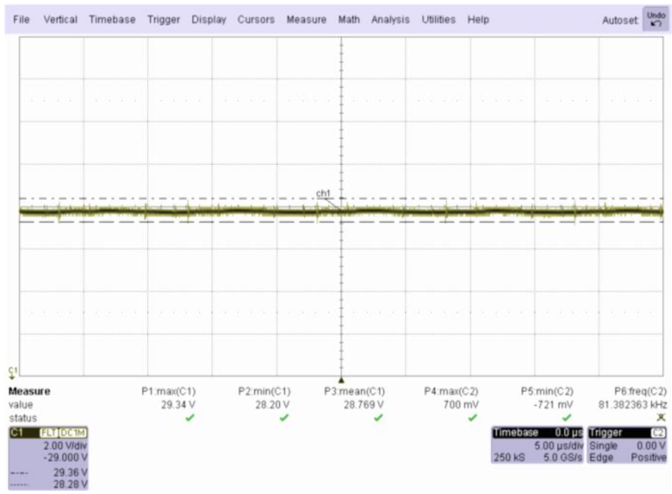

Fig. 8. High frequency spikes and voltage ripple of output voltage

Some of achieved parameters can be seen in Fig. 9. and Fig. 10. Output voltage was decreasing only in range of few millivolts. Total current capability was measured only for 80 A, due to limited power of electronic load. According to design, the maximum reachable current should be 90 A. On Fig.10. there is shown overall efficiency and input and output power. The efficiency is highest from 30 to 50 A and then it is decreasing.

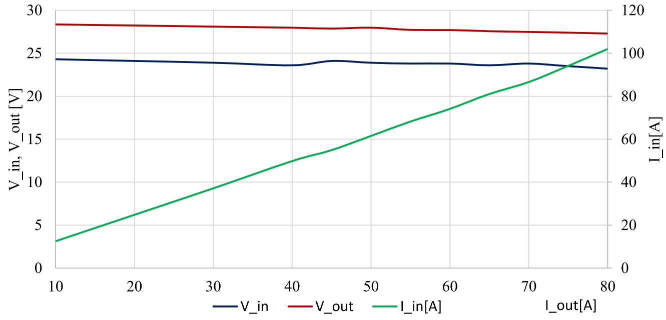

Fig. 9. Measured input and output voltages and currents

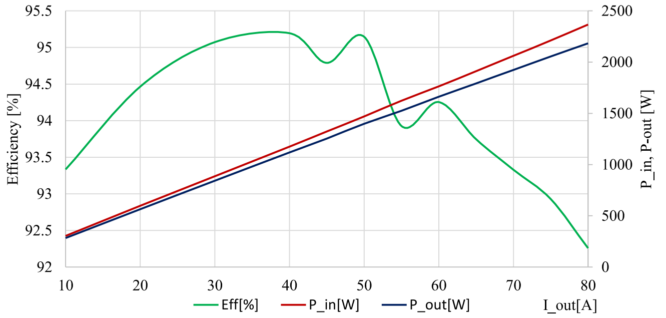

Fig. 10. Measured input and output power and achieved efficiency

The input and output traces were unmasked, because of soldered additional layer with wires to ensure that traces can carry higher currents. This can be seen on Fig. 11. The PCB is made of six layers and the thickness of top and bottom layer was increased to 70 um. It is recommended to keep all gate drive traces in sufficient distance from sensitive signal as current sense traces, measuring amplifiers and other signal traces. In this project all high frequency switching traces were in inner layer.

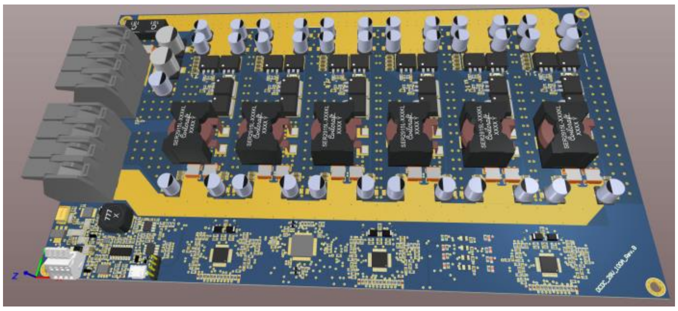

Fig. 11. Model of DC-DC convertor

V. Conclusion

The aim of the work was to design a high power paralleled step-up DC-DC convertor. The convertor is increasing input voltage from 24 V to output 28 V with capability to deliver 90 A of current. Convertor is made of three current controllers which are connected in parallel. This article also explains the main principle of synchronization used for parallelism. The main goal is to explain the basic principal of parallelization of switching DC-DC converters and a way to minimize current sharing error between individual current controllers. Minimum sharing error was achieved at fully loaded converter and it was under 1 %. As current controllers are able to drive two half bridges, the current sharing error between these channels were measured.

Another part of this article is focused on importance of length matching not only between individual channels or convertors, but also between paralleled transistors in half bridge. Inaccurate length matching between two paralleled transistors is causing higher power dissipation at transistor which is connected closer to gate driver conducts more current than the other. Inaccurate length matching causes increase of current sharing error.

Acknowledgment

Research described in this paper was financed by Czech Ministry of Education in frame of National Sustainability Program under grant LO1401. For research, infrastructure of the SIX Center was used. The research published in this submission was financially supported by the Brno University of Technology Internal Grant Agency under project no. FEKT-S-17-4713.

References

[1] Texas Instruments: "Demystifying Type II and Type III Compensators Using OpAmp and OTA for DC/DC Converters - SLVA662" [online]. In: . July 2014, s. 1-16 [cit. 2018-07-31].

[2] Texas Instruments: "LM5170-Q1 Multiphase Bidirectional Current Controller" [online]. In: . Nov. 2016–[Revised June 2017], s. 0-71 [cit. 2018-07-31].

[3] SUN, Juanjuan. Dynamic Performance Analyses of Current Sharing Control for DC/DC Converters. Blacksburg, Virginia, 2007. Dissertation thesis. Virginia Polytechnic Institute.

[4] Chang-Shiarn Lin and Chern-Lin Chen, "Single-wire current-share paralleling of current-mode-controlled DC power supplies," in *IEEE Transactions on Industrial Electronics*, vol. 47, no. 4, pp. 780-786, Aug. 2000. doi: 10.1109/41.857958

[5] Microchip: "MIC45212 Current Sharing Reference Design" [online]. In: . Nov. 2016–[Revised Feb.2017], s. 0-71 [cit. 2018-07-31].

[6] Texas Instruments: "Current Sharing in Redundant Systems" [online]. In: . March. 2010, s. 0-9 [cit. 2018-07-31].

[7] Y. Panov and M. M. Jovanovic, "Loop Gain Measurement of Paralleled DC–DC Converters With Average-Current-Sharing Control," in *IEEE Transactions on Power Electronics*, vol. 23, no. 6, pp. 2942-2948, Nov. 2008.
doi: 10.1109/TPEL.2008.2002955

Optical Disc Segmentation Using Fully Convolutional Neural Network in Retina Images.

Branislav Hesko
Faculty of Electrical Engineering
University of Technology Brno
Brno, Czech republic
Email: hesko@vutbr.cz

Vratislav Harabiš
Faculty of Electrical Engineering
University of Technology Brno
Brno, Czech republic
Email: harabis@vutbr.cz

Radim Kolář
Faculty of Electrical Engineering
University of Technology Brno
Brno, Czech republic
Email: kolarr@vutbr.cz

***Abstract*—This paper focuses on optic disc segmentation, which is one of the main steps in glaucoma diagnostics. A novel method, based on semantic, pixel-wise segmentation using the fully convolutional network is applied to the RIM-ONE dataset. This approach is advantageous because no additional preprocessing or postprocessing is needed. Moreover, results are promising, reaching mean IOU at about 0.7 and thus can compete with state of the art methods. The only disadvantage lays in the need of training dataset of sufficient size.**

I. Introduction

Ophthalmoscopy is a noninvasive method to examine eye diseases. One of the most common diseases is glaucoma, associated with high intraocular pressure. Standard glaucoma detection procedure employs manual optic disc and cup detection. The optic disc is the area of the retina, where rods and cones are not present, only optic nerve, which is leaving eye here. It is also an entry point for retinal blood vessels. Optic cup is a part of the disc with the central depression. There are several clinical applications that are using disc properties. Mostly, cup to disc ratio is significantly correlated with glaucoma disease, when eye suffers glaucoma, its cup to disc ratio significantly increases, which is mostly caused by an increasing cup area. Therefore, optic disc and cup segmentation are an important step in glaucoma diagnostics. [6]

There are various automatic methods for optic disc segmentation, mostly level set methods, active contours, template matching or different versions of Hough transform [1], [2]. In this work, a novel and modern approach to optic disc segmentation are applied. Using fully convolutional neural network, pixel-wise semantic segmentation may be obtained. Moreover, the chosen architecture allows manipulating with datasets of limited size, as we are only fine-tuning pretrained network.

II. Dataset

With a typical computer setup, a user can afford image sizes of about $[512 \times 512]$ pixels with a reasonable computing time on a modern GPU. But, ophthalmological data are acquired at higher resolutions. One possible solution is to work with low sized images. Despite, we are using RIM-ONE dataset [4] with images of size $[1072 \times 1424]$ pixels, even if there are databases that contain images of sufficiently low sizes, like STARE or DRIVE, but these can be considered outdated. The whole database contains 159 stereoscopic images. We split each stereoscopic image into two distinct images with the same mask. Both images are slightly translated. Other solution would consist of image downsampling to lower sizes. As we would like to utilize the maximum amount of information, we employ cropping approach. Each image is processed by regions of size $[512 \times 512]$ pixels. These regions are overlapping and the whole image is divided into ≈ 200 regions. Therefore, each pixel is segmented multiple times and to obtain effective segmentation for each pixel, count map is constructed for each image. Final pixel segmentation is then computed by taking mean region segmentation result.

The RIM-ONE dataset is not uniform. It contains differently illuminated retina images, the disc has different shapes and sizes. Originally, the dataset was split into glaucoma and healthy samples, but in this work, both groups are merged together. As an example of a great dataset variability, some of its images are inserted below [4]:

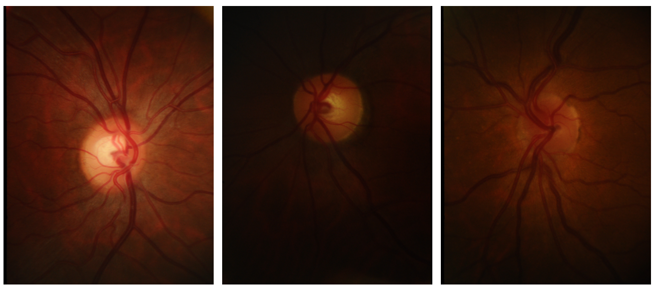

Fig. 1: Different training data images. High variability is visible.

III. Network architecture

The chosen architecture is composed of an encoder and decoder part and is called SegNet. Both encoder and decoder are symmetric, thus they contain the same number of layers. There are various architectures based on encoder and decoder chaining. We may mention U-Net[3] with a direct link between encoder and decoder or PSPnet based on ResNet architecture with a high number of layers. On the contrary, SegNet employs a novel type of layers: unpooling layers.

A. SegNet architecture

The general SegNet architecture is shown on the figure 2:

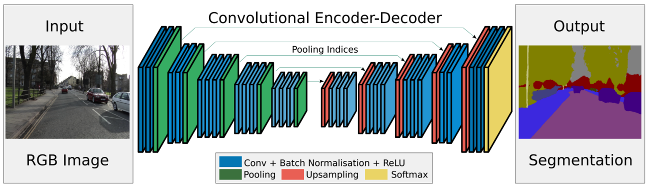

Fig. 2: SegNet architecture.

One of the main SegNet advantages is its encoder, which is directly VGG (very deep convolutional network [5]). It is fully convolutional with increasing number of feature maps in each layer. The output's size is 4096. For general classification problems, the output of the network may be combined with a classifier, but in this case, decoder network is added. There are multiple VGG versions, according to the number of layers and we are using VGG-19 version with batch normalization in each layer. According to the literature, this input preprocessing enhances training and prevents overfitting. Moreover, each layer uses convolutional layers with zero padding, thus input and output are the same sizes. Size reduction occurs on pooling layers of size 2×2, where the output is two times down-sampled. Max pooling is applied. After each convolutional layer, activation function ReLU is applied. In the decoder network, layers are organised symmetrically with the same number of feature maps as in encoder part. Convolutional layers are the same, they also preserve input size. Pixelwise segmentation needs the output of the same size as input. Therefore, a new type of layer is used: unpooling layer. This layer upsamples the result. Based on the symmetry, pooling indices from the corresponding pooling layer are stored. Then, unpooling consists of upsampling and storing values only at the pooling indices. Other indices remain zero. With a similar result, bilinear extrapolation may be used, but it shows up, that unpooling via indices reaches better results. Finally, softmax layer as a classifier is used. FInal output consists of two feature maps, one for the background, the second for the optic disc. For out two class problem, ie. background and disc, softmax may be replaced by a simple maximum operation from these two output feature maps. [7], [8]

B. Overfitting prevention

The biggest deep learning problem lays in overfitting. The VGG alone has multiple millions of parameters [5]. In general, it would be possible, that the network will adapt to training examples and instead of learning the optic disc segmentation problem, learning all training examples would happen. The problem is even bigger for small sampled datasets. Therefore some methods to prevent overfitting are adapted:

- Batch normalization is a method, where, the input of each convolutional layer is subtracted by its mean and divided by standard deviation. This helps to achieve lower error rates while speeding up training and preventing overfitting. [9]
- Cross-validation is one of the most currently used methods. Dataset is divided into training, validation and test set. The test set is used for final evaluation, while validation is taken as a criterion for training evaluation and when to stop. It shows, how the currently trained network is able to generalize. Finally, the training set is used to fit parameters.
- Data augmentation is the last used method. Convolutional networks are susceptible to geometric transformations. For example, translation by one pixel may significantly change the output. These effects are partially solved by data augmentation. Training dataset is enlarged by various transformations, like rotation, translation or scaling, making new training samples. Moreover, this procedure provides better results for small datasets. [3]

Even with these preventing methods, our network suffers from inexplicable oscillations of the validation dataset results. Therefore, we train a certain amount of time and then pick the best result on the validation set.

IV. Results

The whole segmentation was implemented in Python programming language and PyTorch framework. The entire dataset is put together, without taking in count whether it contained a healthy or glaucomatous eye. Moreover, images are randomly split into training, validation and testing sets with counts given by ratio: (70%, 10%, 20%). Afterwards, the network is trained with the following settings:

- Loss function - Cross entropy defined as [5]:

$$H = -\frac{1}{M \cdot N} \sum_{i=0}^{N} \sum_{j=0}^{N} p_{i,j} \cdot \log(q_{i,j}), \qquad (1)$$

  with $p_{i,j}$ as true label at pixel position i, j and $q_{i,j}$ predicted probability and M, N image sizes.
- Optimizer - gradient descent method: Nestorov Momentum.
- Momentum value: 0.9.
- Learning rate: exponentially decaying, starting from 0.0025.
- Maximum number of epochs: 50.
- Filter size in convolutional layers: $[3 \times 3]$.
- VGG weights: pretrained on the ImageNet dataset.
- Train batch size - the number of images processed at the same time: 2.

Due to the cropping strategy, each training epoch, ie. passing through all training data takes about two hours. In each epoch, validation set is evaluated twice and corresponding weights with the score are stored. Afterwards, training lasts about 10 epochs and the best validation score is picked as final network configuration. Finally, testing images are passed through the network and their segmentation is used to evaluate the results. On the validation set, the network performs robustly, which can be seen from the figure 3.

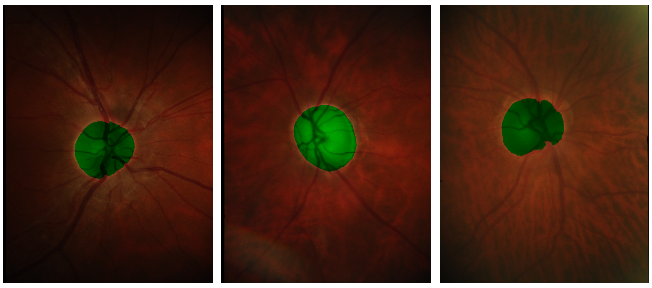

Fig. 3: Segmentation result on the validation images. The network performs well on the first two images, while on the last image, a part of the disc is missing.

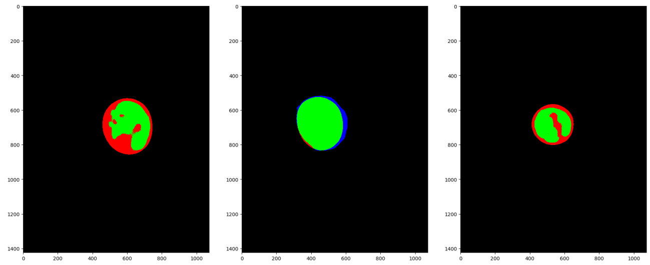

Fig. 5: Ground truth mask merged with the segmentation result. Green color represents correctly classified pixels, red color false negative and blue color false positive pixels. The third image segmentation caught the surrounding structure.

A. *Persisting problems*

On some images in both validating and testing sets, the method does not converge to the ground truth segmentation and there are two common problems, which are shown in the figure 4:

- Disc border is not clear and resulting segmentation catches also disc's neighbourhood. Additional post-processing is then needed and there are two possible solutions. First, when the disc is strictly delimited, a correction would consist of labelling all segmented objects and picking up the biggest and most round.
- In the feature map for disc segmentation, the disc is only partially segmented. This results in disc only partially segmented. There is a simple solution because it shows up, that feature map for background segmentation is not influenced and a simple Otsu threshold improves the result.

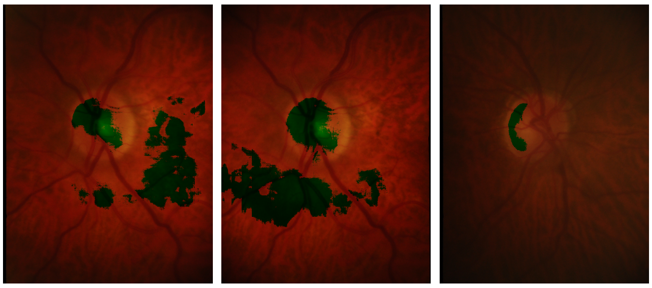

Fig. 4: Segmentation result on the validation images. All of these three images would need additional postprocessing designed above.

Statistical evaluation is then performed on testing set, which will explore generalization properties of the network.

V. Evaluation

For the selected network, the testing set is previously unknown. Generalization is defined as the ability of an algorithm to handle new data. First, we merged ground truth mask with the segmented one and inserted it into the figure 5. We may conclude, that the network generalizes well because both ground truth and segmented masks are almost identical.

Afterwards, several statistical measures are computed, which can be then compared with the state of art methods: sensitivity, specificity, intersection over union, dice coefficient and accuracy. Sensitivity can be computed as [10]:

$$\text{sensitivity} = \frac{TP}{TP + FN}, \tag{2}$$

where TP are correctly classified disc pixels and FN are pixels misclassified as background. Specificity is given by [10]:

$$\text{specificity} = \frac{TN}{TN + FP}, \tag{3}$$

here TN are pixels correctly classified as background and FP are pixels falsely classified as background. Finally, accuracy is similarly defined as [10]:

$$\text{accuracy} = \frac{TP + TN}{TP + TN + FP + FN}. \tag{4}$$

In general, sensitivity and specificity are used in diagnostics to evaluate false positive and false negative impact on misclassification. Here, they are evaluated for pixels of each image and overall specificity(sensitivity) is given as mean value across all images. Intersection over union is defined simply as [11]:

$$\text{IOU} = \frac{GT \cap S}{GT \cup S}, \tag{5}$$

where GT is ground truth mask and S segmented mask. IOU reaches 1 for perfect segmentation. Finally, dice coefficient is given by [11]:

$$\text{DICE} = \frac{2 \cdot |GT \cap S|}{|GT| + |S|}. \tag{6}$$

These statistical measures are calculated and put into a table for testing set and informationally also for validation set.

TABLE I: Statistical scores of the method.

Set	IOU	DICE	Accuracy	Sensitivity	Specificity
Test	0.68	0.77	0.98	0.73	0.99
Validate	0.75	0.83	0.99	0.77	0.99

Based on these results, it is possible to deduce, that method performs quite well. IOU and sensitivity show what should be improved. When comparing to other works [12], [13], where authors achieved mean IOU at 0.7 and 0.8 respectively, we have worse results concerning IOU. This may be caused by a downsampling of images into a small region in the mentioned works. And if we look at each image individually, we are able to find out, that only a subset of images suffers from bad segmentation, the majority of the images reaches sufficiently high values of IOU. This can be seen from the figure 6. Moreover, we have divided datasets into three distinct groups, while in mentioned works, evaluation was done on the validation set.

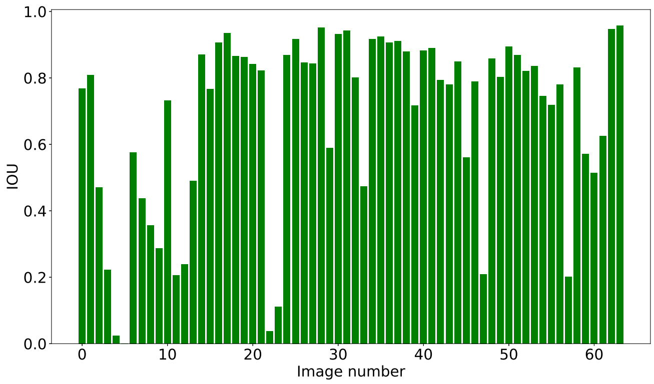

Fig. 6: IOU score reached by each image. This figure shows that majority of images has sufficiently high IOU score, except images where additional treatment would be necessary.

VI. Conclusion

In this paper, a novel algorithm for optic disc segmentation has been presented. It shows up to be a promising alternative to currently used methods. Overal algorithm reaches mean intersection over union at 0.68 without any data preprocessing or postprocessing. Sensitivity is also lower and reaches about 0.73 and other parameters are sufficiently high. Several persisting problems were revealed and possible improvement described. In the future, optic cup segmentation would be needed as well, to assess cup to disc ratio, which is related to glaucoma diagnostics.

References

[1] P.S. Mittapalli and G.B. Kande, *Segmentation of optic disk and optic cup from digital fundus images for the assessment of glaucoma*, Biomedical signal processing and control, 12p., 2016.

[2] S. Roychowdhury et al., *Optic Disc Boundary and Vessel Origin Segmentation of Fundus Images*, IEEE Journal of Biomedical and Health Informatics, 12p. 2015.

[3] O. Ronneberger et al., *U-Net: Convolutional Networks for Biomedical Image Segmentation*, MICCAI2015, 7p., 2015.

[4] F. Fumero et al., *RIM-ONE: An open retinal image database for optic nerve evaluation*, CBMS, 2011.

[5] K. Simonyan and A. Zisserman, *Very Deep Convolutional Networks for Large-Scale Image Recognition*, Computer Vision and Pattern Recognition, 14p., 2014.

[6] D.W.K. Wong et al., *Level-set based automatic cup-to-disc ratio determination using retinal fundus images in ARGALI*, Annual International IEEE EMBS Conference, 4p., 2008.

[7] V. Badrinarayanan. et al., *SegNet: A Deep Convolutional Encoder-Decoder Architecture for Image Segmentation.* IEEE Transactions on Pattern Analysis and Machine Intelligence, 39(12), pp.2481-2495, 2017.

[8] V. Badrinarayanan. et al.,*SegNet: A Deep Convolutional Encoder-Decoder Architecture for Robust Semantic Pixel-Wise Labelling*, 14p., 2015.

[9] S. Ioffe and Ch. Szegedy, *Batch Normalization: Accelerating Deep Network Training by Reducing Internal Covariate Shift*, CoRR, 11p., 2015.

[10] A. Fenster and B. Chiu, *Evaluation of Segmentation algorithms for medical imaging.*, Engineering in Medicine and Biology, 5p., 2005.

[11] K.H. Zou et al., *Statistical Validation of Image Segmentation Quality Based on a Spatial Overlap Index*, Scientific reports, 11p., 2004.

[12] A. Sevastopolsky, *Optic Disc and Cup Segmentation Methods for Glaucoma Detection with Modification of U-Net Convolutional Neural Network*, 13p. 2014.

[13] J. Zilly et al., *Glaucoma detection using entropy sampling and ensemble learning for automatic optic cup and disc segmentation*, Computerized Medical Imaging and Graphics, vol. 55, pp. 28–41, 2017.

EBG Structure for both On-Body and Off-Body Communication

Martin Kokolia
Department of Radio Electronics
Brno University of Technology
Brno, Czech Republic
xkokol01@stud.feec.vutbr.cz

***Abstract*—This paper is proposing dual usage of frequency selective surfaces composed of electrical band bap structures. In combination with electrically small antennas the proposed system can utilize lower frequencies of UHF band that are less compromised by proximity of the human body tissue. Periodic structure is designed in a way that at lower frequency band the surface has very high surface impedance to minimalize effects of proximity of the human body to support off-body communication and on the other band the surface supports surface waves for on-body communication.**

Keywords—EBG, FSS, HMMPA, Electrically small atennas, Near body communication

I. INTRODUCTION

For past two decades there has been a strong trend to utilize microwave systems on textile substrate in wearable applications. Those offer opportunities for a lot of medical or security systems that are conveniently integrated into the cloth. Every design in this field struggles with negative impact of both high RF losses in the textile substrate, mechanical deformations while the cloth is being worn and most profoundly, the proximity of the human body [1-8].

Most of designs in published papers are dealing with these problems simply by using planar antenna with a large ground plane that should shield antenna from the body. Those antennas are however quite sensitive to changes of the substrate thickness. Those must be expected at wearable applications and system that is constantly changing operational frequency is not very usable and planar UWB antennas usually cannot use large ground plane as shielding, therefore suffering significant decrease in terms of actual radiation efficiency.

In last years the EBG structures became quite popular solution for a lot of usual issues with antennas. Those can be used for example to reduce side lobes of the radiation patterns and improve main lobe gain by use as superstrate [9,10], increase isolation among antennas on the same substrate [11] and much more.

EBG structures are composed of periodically repeated simple cells. Those typically are used at single frequency band at which the structure produces desired behavior. Usually those are not used at any other frequency bands, but some designs have desired proprieties repeated at several frequency bands.

Goal of this paper is to design simple EBG cell that have two kinds of desired behavior at two separated frequency bands. Then this structure can minimalize negative effects of the proximity of the human body on the off-body communication at the first frequency band and effects on the on-body communication at the other frequency band.

To make the most challenging scenario, let us assume use on surface on the Kevlar-based bullet-proof vest that can even have pouches with an additional equipment on top of it that can block some area of the vest. That would most certainly be major issue with any traditional communication system.

II. DESIGN OF THE FREQUENCY SELECTIVE SURFACE

First step was to design a periodic EBG structure to support on-body and off-body communication. It is desired to chose reasonably low frequencies in the UFH band that are usually not so susceptible to proximity of the human body and dimensions are bit more robust, so antennas should not be much affected by slight deformations that are to be expected while being worn.

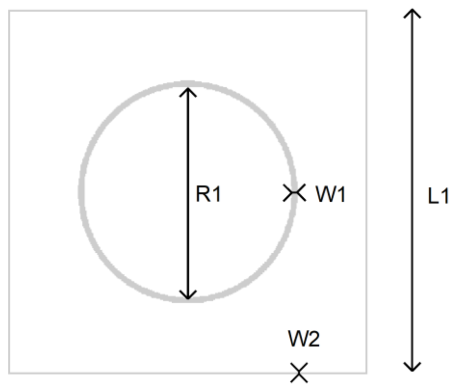

Fig. 1. EBG Cell

At the Fig.1 is shown the proposed EBG cell composed of copper foil on generic model of polyester textile material of thickness equal to 2 mm and relative permittivity equal to 1.2. Simplistic and symmetric design is again desired for mechanical durability of the resonant frequencies.

TABLE I. DIMENSIONS OF THE EBG CELL

Symbol	*Value*	*Unit*
L1	180	mm
R1	55	mm
W1	3	mm
W2	2	mm

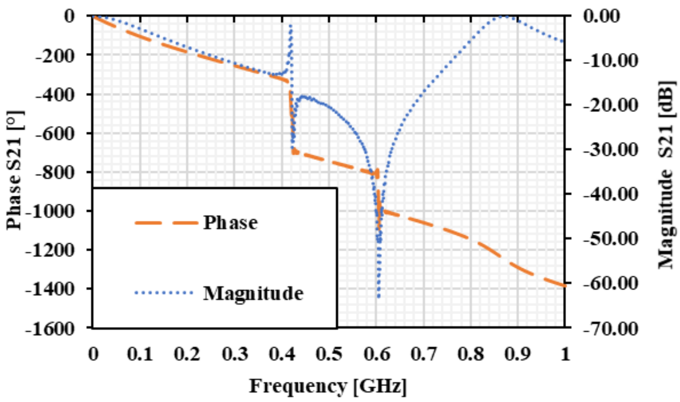

Fig. 2. Reflection coeficient phase and magnitude

As shown at the Fig. 2, the designed cell resonates at 415 MHz. As can be seen at the Fig. 3, this band gap is between the first (magnetic) and second (electrical) mode, that is not supporting surface waves and have high impedance. Another resonation is at 605 MHz with low impedance. At 880 MHz the cell has the lowest attenuation. These results have to be confired by actuall passbands at the diespersion diagram of the periodic structure.

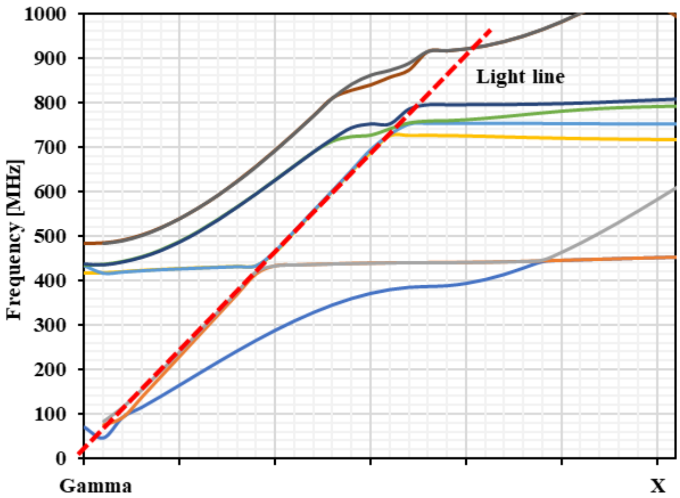

Fig. 3. Dispersion diagram of the EBG cell

At the Fig. 3 there is depicted dispersion diagram of the designed EBG cell. This again shows that at about 430 MHz there is narrow resonance. We can also see that the third mode gets the same slope as the first mode at the desired frequency, which indicates the resonance. There is a very small gap between the first and the second mode. The second band of interest in aproximetly from 810 to 910 MHz. This band is between the eight and the nineth mode and thus provides artificial magnetic conductor that supports surface wave propagation. Therefore this band is usefull for on-body comunication.

III. DESIGN OF DIPOLE ANTENNA

For purpose of the off-body comunication the miniaturized dipole atenna was chosen. Two arms of the dipole are folded in a way that provides reasonable gain while minimizing the dimensions. The design is depicted at the Fig. 4. This basic design provides almost omnidirectional radiation at 450 MHz at free space. While placed at the designed frequency selective surface, the operation frequency of the antenna is 415 MHz.

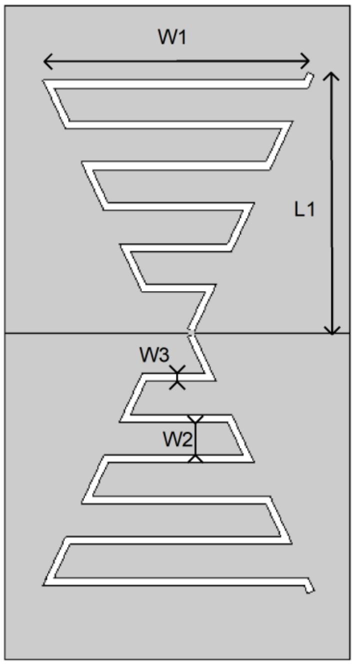

Fig. 4. Eletrically smal dipole atenna

TABLE II. DIMENSIONS OF THE EBG CELL

Symbol	*Value*	*Unit*
L1	100	mm
W1	100	mm
W2	10	mm
W3	3	mm

At the Fig. 5 and 6 there is show frequency response of the reflection coeficient and overal efficiency of the antenna. It is clear, that while antenna itself resonates at several frequencies, it is able to radiate only at the high impedance frequency of the frequency selective surface.

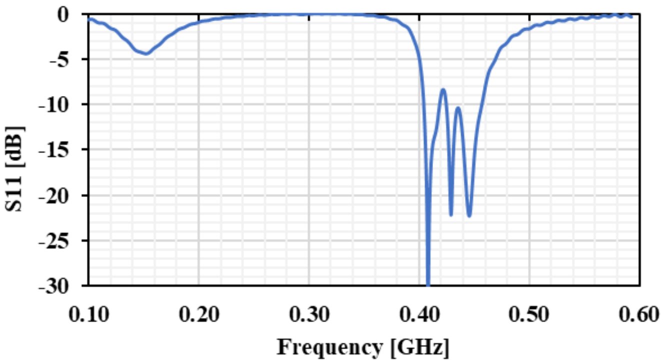

Fig. 5. Dependancy of the reflection coeficient of dipole antenna

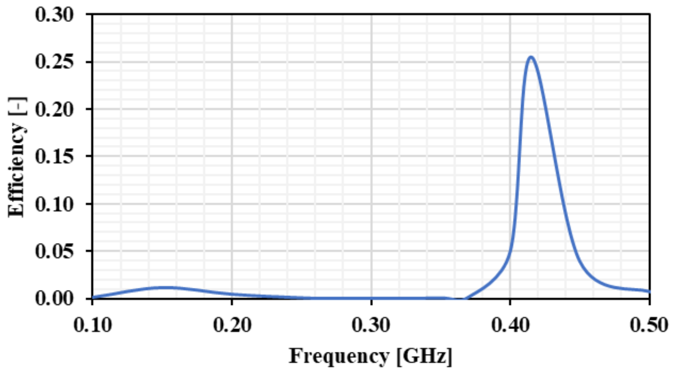

Fig. 6. Dependancy of the overal efficiency of dipole antenna

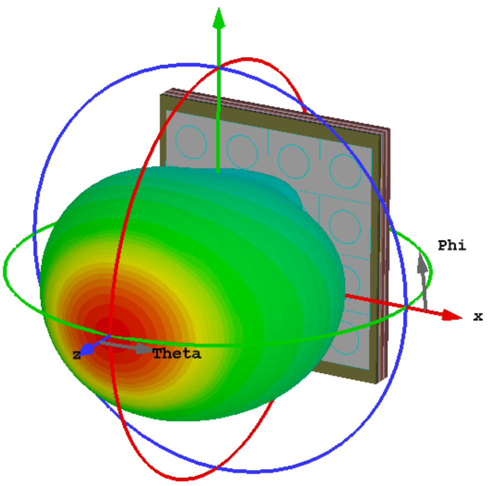

Fig. 7. Radiation diagram of the dipole antenna

As shown at Fig. 7 the radiation diagram is strongly directional outward of the furface. The realized gain is equal to 3.8 dBi with front to back ratio equal to 42 dB. Antenna clearly provides usable efficiency and wide angle of radiation.

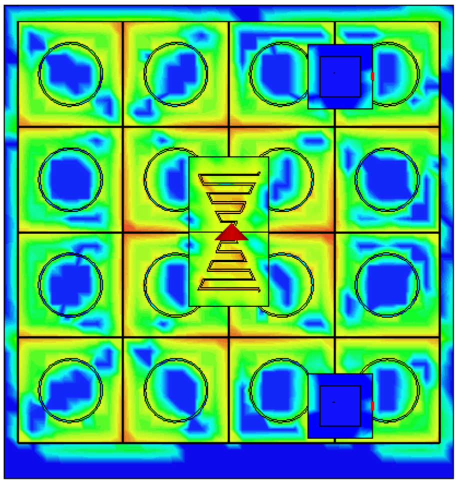

Fig. 8. E-field generated by the dipole antenna at 420 MHz

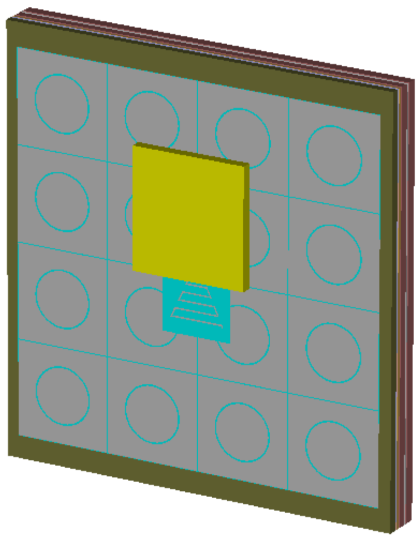

Fig. 9. Obstructed atenna with EBG structure

The Fig. 9 shows simulation with an obstacle made of iluminium placed 10 mm above the antenna. This simulates real-life scenario where the proposed system is for example partialy covered by some electronical device. Normally this would severe decrease of the efficiency of the antenna. As shown at the Fig. 10 the radiation patter is hardly changed at all. The maximal gain is now equal to 3 dBi. This robustnes of the system originates from the behaviour of the FSS. The periodic cell structure does not support propagation of the surface waves allong the surface is is radiating them outwards. Thefeore the antenna is practicaly serving as mere feeding of the structure that radiates as whole.

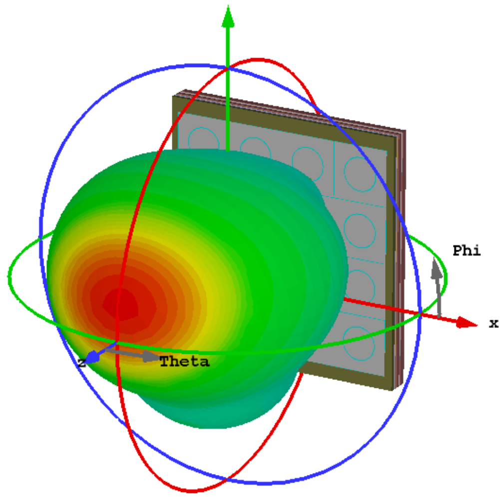

Fig. 10. Radiation diagram of an obscured dipole antenna

IV. DESIGN OF HMMPA

For purpose of the on-body communication it is desired to design an antenna with a vertical polarization relative to the plane of the body. The higher mode microstrip patch antenna is chosen for it is both electrically small and vertically polarized. This makes it ideal planar antenna for on-body communication.

Design of this antenna consists of three conductive layers that are separated by two layers of the textile substrate. The composition and geometry are as shown at the Fig. 11. The first layer is the patch antenna, that is fed by a current probe from the microstrip line from the middle layer. In proximity of the feeding point there are two shorting connections through both layers of the substrate to the bottom conductive layer that is a grounding plate.

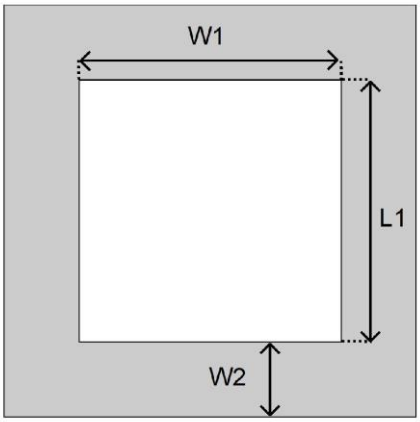

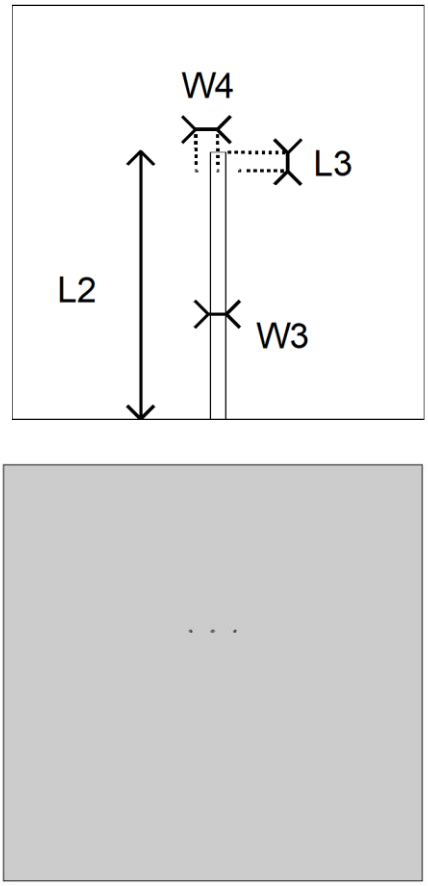

Fig. 11. HMMPA design

TABLE III. DIMENSIONS OF THE EBG CELL

Symbol	***Value***	***Unit***
L1	70	mm
L2	60	mm
L3	5	mm
W1	70	mm
W2	20	mm
W3	4	mm
W4	6	mm

Designed antenna is about 60% smaller than conventional patch antenna of the same operation frequency with realized omnidirectional gain of 3 dBi on the horizontal plane

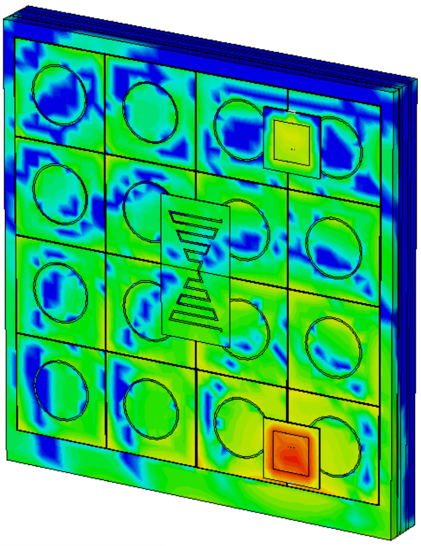

Fig. 12. E-field emitted by HMMPA at 880 MHz

V. Simulation of the System

Final systems composition can be seen at Fig. 12. The dipole antenna is placed in the middle with two on-body communication antennas are placed 50 cm apart. Bellow the periodic EBG surface there is simple model of the Kevlar layer with thickness of 20 mm. Bellow that is a standard model of the human tissue composed of layers of the skin, muscle, fat and bones. Simulations should show results of simultaneous functionality of the both antennas as well as the specific absorption rate of the power emitted by antenna near the human body. System should also be able to functionate also during flexible deformations of the whole systems while being worn.

At the Fig. 12 there is depicted E-Field emitted by the on-body communication antenna at 880 MHz. It is obvious that there are surface waves propagating along the EBG surface. The propagation losses between two antennas placed 50 cm apart is are shown at the Fig. 13. At the 880 MHz the losses basically equal to the free space losses. Antennas have gain about 3 dBi in the direction of the propagation, therefore the propagation path has additional losses of about 6 dB. This result is significantly better than if the vertically polarized wave was propagating along the human body only.

TABLE IV. Simulated SAR

Frequency	*1 gram tissue [W/kg]*	*10 gram tissue [W/kg]*
415	0.03	0.02
880	0.02	0.01

As shown at the table IV. the SAR is reduced by more than 95% compared to antennas radiating without the EBG structure. Without the EBG structure basically all energy would be absorbed by the body tissues however. These values are still approximately 5 times higher than can be achieved by conventional planar antennas with ground plane like patch antenna, but still well bellow the safe limits.

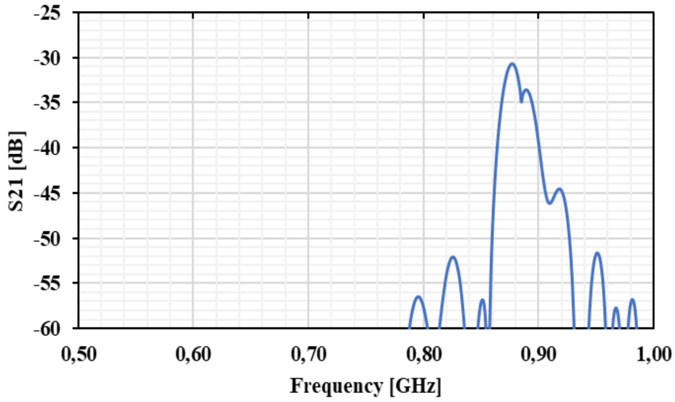

Fig. 13. EBG Cell

Even if there was a conductive or the dielectric obstacle in between the antennas, the losses in the propagation are virtually unchanged even if the obstacle was as close as 2 mm above the periodic structure. This shows that the wave is propagating almost solely inside the periodic structure.

VI. Conclusion

The presented design consists of slightly modified components that are already known and proven to be functional and by combining them very promising results are achieved. While simulated on the model of the human body and even with layer of Kevlar or additional obstacle above the off-body antenna or in between the on-body antennas has very little effect on the efficiency of the connection.

This system has proven to be reasonably robust even to curvature of the human body and additional deformations. The system can be further expanded for on-body communication around the torso or from leg to torso etc. Next step then is to manufacture the prototype to be measured on the phantom model of the human tissue and later to be measured on an actual person.

Acknowledgment

The research was supported by the Czech Ministry of Education by the National Sustainability Program grant LO1401.

References

[1] S. Sankaralingam and B. Gupta, “Effects of bending on impedance and radiation characteristics of rectangular wearable antenna utilizing smart clothes”, Microwave and Optical Technology Letters, vol. 54, no. 6, pp. 1508-1511, 2012.

[2] X. Tong, C. Liu, X. Liu, H. Guo, and X. Yang, “Switchable ON-/OFF-Body Antenna for 2.45 GHz WBAN Applications”, Antennas and Propagation, IEEE Transactions on, vol. 66, no. 2, pp. 967-971, 2018

[3] H. Rogier, S. Agneessens, F. Declercq, A. Dierck, W. Joseph, M. Moeneclaey, L. Vallozzi, P. Van Torre, and J. Vanfleteren, “Textile antenna systems for positioning and off-body communication”, in IET Conference Proceedings, 2013

[4] C. Hertleer, H. Rogier, L. Vallozzi, and L. Van Langenhove, “A Textile Antenna for Off-Body Communication Integrated Into Protective

Clothing for Firefighters", Antennas and Propagation, IEEE Transactions on, vol. 57, no. 4, pp. 919-925, 2009.

[5] E. S. Florence, M. Kanagasabai, and G. N. M. Alsath, "An investigation of a wearable antenna using human body modelling", Applied Computational Electromagnetics Society Journal, vol. 29, no. 10, pp. 777-783, 2014

[6] P. Vašina, "Textile SIW Rectangular Ring-slot Antennas for Off-body Communication", in Proceedings of the 22st Conference STUDENT EEICT 2016, pp. 343-347

[7] S. Yan and G. A. E. Vandenbosch, "Radiation Pattern-Reconfigurable Wearable Antenna Based on Metamaterial Structure", Antennas and Wireless Propagation Letters, IEEE, vol. 15, pp. 1715-1718, 2016

[8] A. Y. I. Ashyap, Z. Zainal Abidin, S. H. Dahlan, H. A. Majid, S. M. Shah, M. R. Kamarudin, and A. Alomainy, "Compact and Low-Profile Textile EBG-Based Antenna for Wearable Medical Applications", IEEE Antennas and Wireless Propagation Letters, vol. 16, no. 99, pp. 2550-2553, 2017

[9] Q. Bai and R. Langley, "Wearable EBG antenna bending", in European Conference on Antennas and Propagation, EuCAP 2009, Proceedings, 2009, pp. 182-185

[10] R. Gupta and J. Mukherjee, "EFFICIENT HIGH GAIN WITH LOW SIDELOBE LEVEL ANTENNA STRUCTURES USING CIRCULAR ARRAY OF SQUARE PARASITIC PATCHES ON A SUPERSTRATE LAYER", Microwave And Optical Technology Letters, vol. 52, no. 12, pp. 2812-2817, 2010.

[11] X. Yang, Y. Liu, Y. -X. Xu, and S. -X. Gong, "Isolation Enhancement in Patch Antenna Array With Fractal UC-EBG Structure and Cross Slot", Antennas and Wireless Propagation Letters, IEEE, vol. 16, pp. 2175-2178, 2017

Methods for respiration estimates using single lead ECG

Martin Kralik
Faculty of Electrical Engineering
Brno University of Technology
Brno, Czech republic
Email: kralikmartin@feec.vutbr.cz

Jiri Kozumplik
Faculty of Electrical Engineering
Brno University of Technology
Brno, Czech republic
Email: kozumplik@feec.vutbr.cz

***Abstract*—This paper deals with the problematic of respiration estimates from single lead electrocargiogram (ECG) and their possible use for sleep apnoea detection. Two different methods are used, each using different approach. RSA method utilises physiological ties between respiration and cardiac activity. EDR method is using changes in ECG signal caused by chest movements. Both methods are used on real data from patients suffering from sleep apnoea syndrome and are their results are subjectively compared in the conclusion.**

***Keywords*—respiration, electrocardiography, sleep apnoea syndrome**

I. Introduction

There is no need to question the importance of sleep in human life. In modern world, multiple factors affect the quality of sleep negatively, causing sleep disorders. These can decrease quality of life in a form of depressions, sleepiness and others. Of those disorders, insomnia is probably the most known in public, but breathing problems during sleep have high prevalence in population as well, with sleep apnoea (apnea) syndrome (SAS) being the most common. According to [1], up to 10 % of population over 65 years old suffers from SAS, but this number is probably even higher.

Although the area of sleep disorder diagnostics is well known, it requires physical examination in sleep laboratory. This process is not only expensive and time consuming , but also brings certain level of discomfort to the patient. Due to these facts, alternative methods of examinations and SAS detection are being found. One of these methods utilizes long term ECG monitoring, trying to acquire information about breathing from ECG signals.

II. Sleep apnoea syndrome

According to American Academy of Sleep Medicine, SAS is described as interruption of ventilation for 10 s and decrease of oxygen saturation by more than 3 %. Golden standard for SAS diagnosis is polysomnography (PSG). PSG is an all night physical examination, during which multiple biological signals are measured. For SAS diagnosis, we are mostly interested in four signals [2].

- Nasal airflow, measured by either thermocouple or piezoelectric sensor placed in a proximity of nostrils.
- Breathing movements of chest and abdomen, measured as changes of volume, using inductance plethysmography.
- Oxygen saturation, measured using pulse oxymeter placed on finger or auricle

We can distinguish two main types of SAS - obstructive sleep apnoea (OSA) and central sleep apnoea (CSA). Each of those has different cause and we can also observe different breathing patterns for OSA and CSA [3].

OSA is more common type of SAS, with prevalence about 10 % with mid aged men, 3 % with mid aged women and up to 17 % with men over 50. OSA is caused by partial or complete blockage of upper airway. Typical phenomenon for OSA is presence of breathing movements in the area of chest and abdomen. Nasal airflow is highly decreased or dissapeared [3]–[5]. Example of such apnoic pause can be seen on Fig.1. Nasal airflow disappears at 6200 s with chest and more noticeably abdomen breathing movements being present. Oxygen saturation is decreasing with approx. 40 s delay.

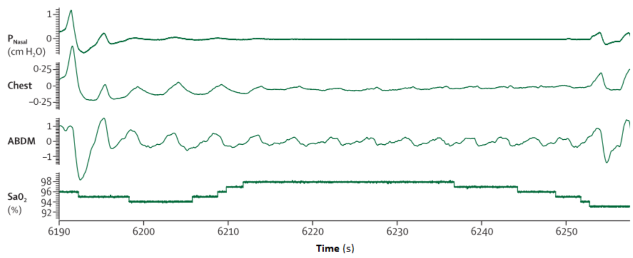

Fig. 1. Example of OSA on PSG record. Pnasal = nasal airflow, Chest = Chest breathing movements, ABDM = abdomen breathing movements, SaO2 = oxygen saturation [4].

CSA is more rare variant of SAS. It's cause is in central nervous system, which stops breathing effort for short time period [3]. On PSG record Fig.2, we can see disappeared nasal airflow (marked Cn.A), together with no breathing effort on chest and abdomen signals.

Previous figures show the importance of informations about breathing for sleep apnoea diagnostics. Since breathing and cardiac activity are tied physiologically, breathing effort can be theoretically estimated using only ECG record, as was mentioned in the introduction. Following chapter describes use of some methods for such estimates.

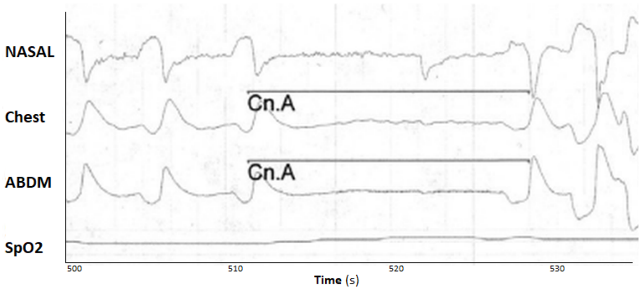

Fig. 2. Example of CSA on PSG record. Nasal = nasal airflow, Chest = Chest breathing movements, ABDM = abdomen breathing movements, SaO2 = oxygen saturation [6].

III. Methods

A. Used data

Data used for ECG-derived respiration estimates come from the Physionet apnea-ECG database. This database contains 70 sleep recordings of ECG signals. 8 recordings also include additional signals - nasal airflow, chest and abdomen movements and oxygen saturation. For this article, data from 4 patients with at least 100 minutes with disordered breathing were used. All records are digitized with 16 bits per sample, 100 samples per second [7], [8].

Two methods of breathing signal estimates are used in this article. First one utilizes the respiratory sinus arrhythmia (RSA) - small changes of heart rate based on respiratory rhythm. Second method is based on ECG voltage fluctuations. During respiration, volume of rib cage changes, which affects ECG signal by low frequency changes of voltage. Furthermore the electrical heart axis changes during respiration cycle as well. Methods based on ECG voltage fluctuations are called ECG derived respiration (EDR) [9], [10].

B. RSA method

Since RSA method is based on variations of heart rate, it is proceeded similarly as with heart rate variability (HRV) analysis preprocessing. The most important part of such preprocessing is QRS detection. Since all patients are laid down and calm during measuring, simplified version of Pan Tompkins detector was used to find QRS complexes. ECG signal was filtered using bandpass FIR filter with limit frequencies 15 Hz and 30 Hz. After squaring the signal, lowpass FIR filter with limit frequency 5 Hz was used. Using MATLAB function for finding local maxima, 99,65 % of QRS complexes was successfully found (Fig.3).

From QRS locations, HRV interval function was created, with each sample being located at the time position of QRS complex and its value representing distance to the next sample. This function was not equidistant and it was resampled to 10 samples per second, using cubic spline interpolation (Fig.4). Resulting function describes variations in heart rate in time. Since heart rate is affected by respiration, this function should also represent respiration.

Comparison of estimated respiration using RSA method and measured signals from nasal sensor and abdomen can be seen on (Fig.5). Figure shows 60 seconds of sleep, which has

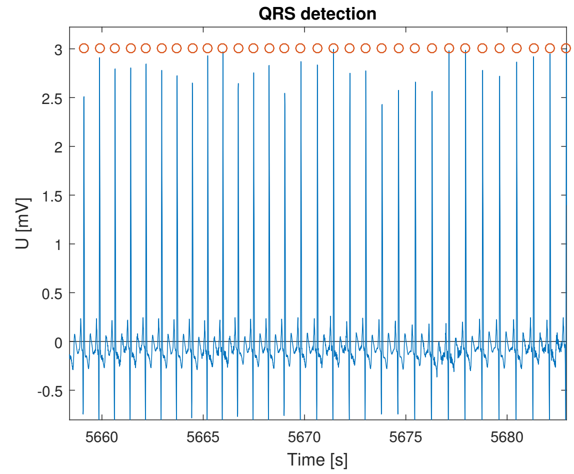

Fig. 3. QRS detection example, red circles are marking detected locations of QRS complexes

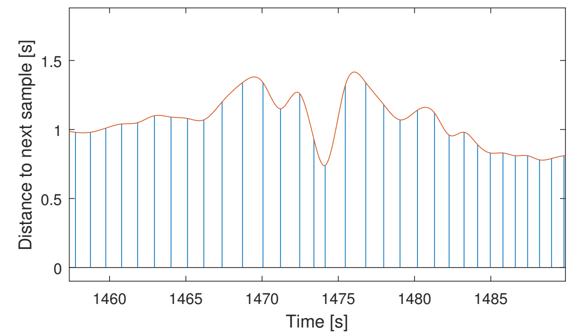

Fig. 4. HRV interval function samples (blue) and equidistant function (orange)

been evaluated as non-apnoea segment. We can see that the respiration obtained with RSA method can be considered as correct.

Since this method should be later used for SSA detection, it should correctly represent breathing pattern during apnoea events. On Fig.6, we can clearly see two apnoeic episodes, first ending at approx 11485 s and second beginning at 11500 s. Estimated respiration signal shows lack of breathing at the same time as the nasal and abdomen signals. This is promising result for future apnoea detection.

C. EDR method

As was mentioned, changes of chest volume and movement of electric heart axis cause small voltage fluctuations in ECG signal. These are mainly visible as changes of local maxima, represented by R waves. The idea of EDR method is to obtain ECG signal envelope. This can be achieved by multiple methods, namely linear filtration, wavelet transform and others. In a case of this paper, simple peak detection was used to locate R waves of ECG and their values. Similarly to the HRV function, locations of these local maxima and their values are not equidistant. For this, spline interpolation was used to

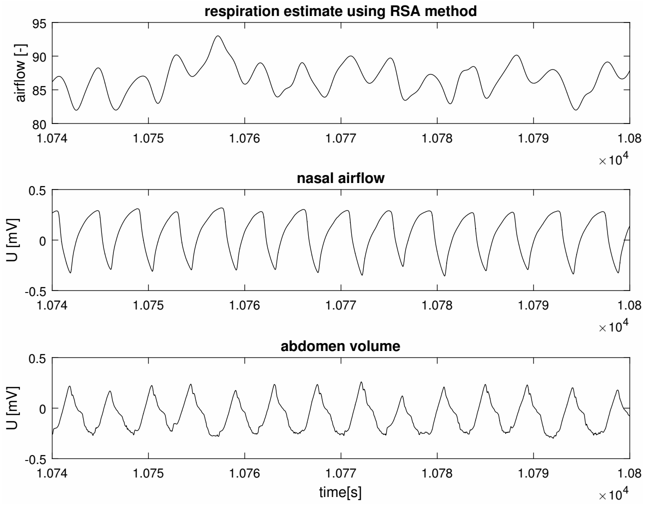

Fig. 5. Comparison of estimated and measured respiration, using RSA method.

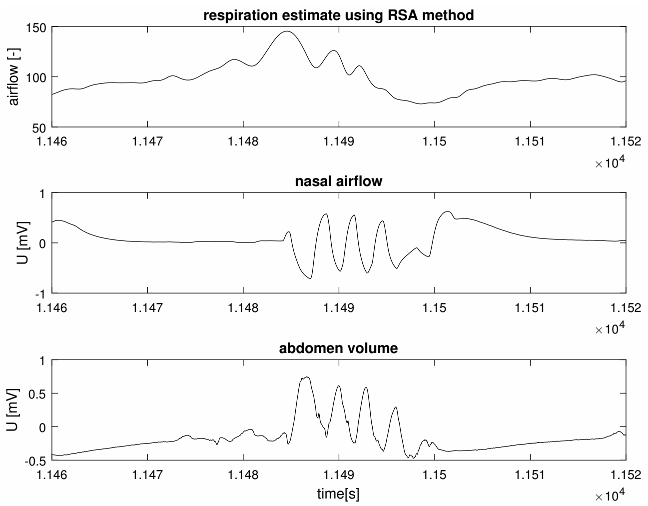

Fig. 6. Comparison of estimated and measured respiration during apnoea, using RSA method.

obtain equidistant signal. Example of calculated envelope with original ECG signal can be seen on Fig.7.

If ECG is measured properly to avoid half-cell potential, low frequency changes in ECG voltage are mainly caused by respiration movements of chest. Thus the calculated envelope should be describing respiration effort. Fig.8 shows 60 s segment of sleep with OSA event in first 30 s. This event is followed by multiple deep breaths, which is visible not only on a chest channel, but also on estimated respiration, in a form of higher amplitude. This could be useful for detection of OSA events, while CSA would be barely visible due to the lack of chest movements.

IV. Conclusion

Two methods of acquiring respiration estimate were used. Both RSA and EDR method show promising results for future apnoea detection. RSA estimates are closely corresponding to

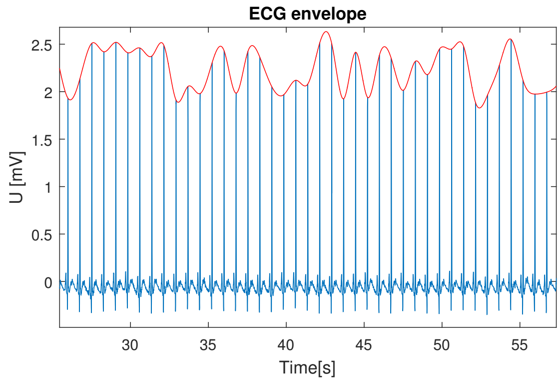

Fig. 7. Segment of ECG signal (blue) with calculated envelope (red).

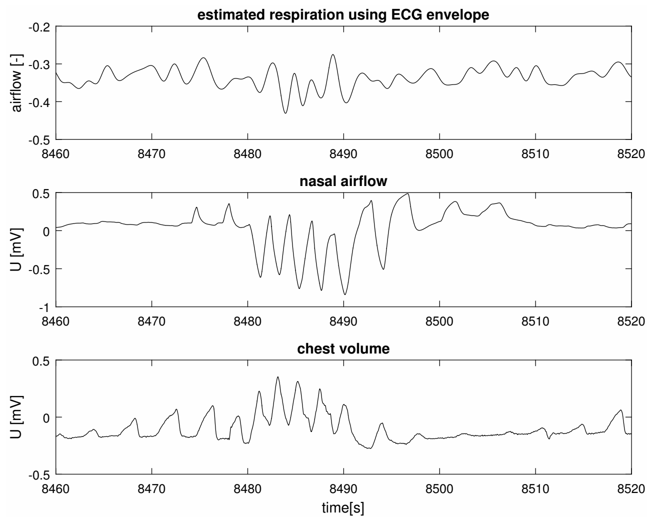

Fig. 8. Comparsion of estimated and measured respiration, using EDR method and ECG envelope.

the nasal airflow, since this method is based on respiration frequency. This could be useful for detection of apnoea event, regardless of its origin, since lack of airflow is typical for both OSA and CSA. There are of course limitations of this method, namely correct QRS detection.

EDR estimates are showing results similar to signals from chest plethysmograph, since this method utilizes changes of chest volume during breathing. As with previous case, there are limitations of this method. Most important would be removal of ECG drift. Due to the fact, that each method is sensitive to different events, their combination could be used not only for SAS detection but also for distinguishing both types of apnoea.

References

[1] J. M. Drazen, "Sleep Apnea Syndrome" , The New England Journal of Medicine, vol. 6, no. 346, 2002.

[2] American Academy of Sleep Medicine, International Classification of Sleep Disorders, 3rd ed. Darien IL: American Academy of Sleep Medicine, 2014.

[3] S. Nevsimalova and K. Sonka, Poruchy spanku a bdeni, 2nd ed. Praha: Galen, 2007.

[4] A. S. Jordan, D. G. McSharry, and A. Malhotra, ”Adult obstructive sleep apnoea”, The Lancet, vol. 383, no. 9918, pp. 736-747, 2014.

[5] P. E. Peppard, T. Young, J. H. Barnet, M. Palta, E. W. Hagen, and K. M. Hla, ”Increased Prevalence of Sleep-Disordered Breathing in Adults”, American Journal of Epidemiology, vol. 177, no. 9, pp. 1006-1014, 2013.

[6] A. Avidan and T. Barkoukis, Review of Sleep Medicine, 3rd Ed. Philadelphia: Elsevier Saunders, 2011.

[7] T. Penzel, G. B. Moody, and R. G. Mark, ”The Apnea-ECG Database”, Computers in Cardiology, vol. 27, pp. 255-258, 2000.

[8] A. L. Goldberger, L. A. N. Amaral, L. Glass, J. M. Hausdorff, P. C. Ivanov, R. G. Mark, J. E. Mietus, G. B. Moody, C. -K. Peng, and H. E. Stanley, ”PhysioBank, PhysioToolkit, and PhysioNet: Components of a New Research Resource for Complex Physiologic Signals”, Circulation, vol. 101, no. 23, pp. e215-e220, Jun. 2000.

[9] E. Helfenbein, C. -hao S. Chien, S. Babaeizadeh, P. Dasari, A. Knik, J. M. Mukherjee, M. King, and L. Shao, ”ECG/EMG-derived respiration during cardiac magnetic resonance imaging”, Journal of Electrocardiology, vol. 45, no. 6, pp. 693-694, 2012.

[10] M. Kamphong, A. Kanitsap, and J. Chaicharn, ”An investigation on parasympathetic nervous system in obstructive sleep apnea syndrome”, in The 6th 2013 Biomedical Engineering International Conference, 2013, pp. 1-4.

Method of Acquisition, Tracking and Pointing Algorithm Analysis for Free Space Optics

Marek Novak, Petr Skryja
Department of Radio Electronics
Faculty of Electrical Engineering and Communication
Brno University of Technology
Technicka 12
616 00 Brno (Czech Republic)
Email: xnovak0m@vutbr.cz, xskryj01@vutbr.cz

***Abstract*—This paper offers a solution for analysis of Free Space Optical (FSO) link terminal with Acquisition, Pointing and Tracking (APT) algorithm. A design of 8 channel sampling and logging device based on Programmable Real-time Unit (PRU) co-processors is performed. Herein presented contribution helps to develop, verify and validate tracking and detection algorithms and to evaluate its performance in changing atmospheric conditions.**

***Keywords*—PRU, APT, FSO, PID**

I. Introduction

Stationary FSO terminals are a valuable technology for point to point communication using lasers [1]. Due to the properties of laser beam propagation through the atmosphere, FSO links are very susceptible to turbulences, mounting mechanics rigidity and precise alignment of both communicating terminals [2], [3]. Therefore, there is a need for a precise APT mechanism, which reduces the influence of those effects to the communication [4].

II. Analyzed System

Figure 1 shows in a simplified way the FSO receiver terminal principle of operation. There are two actuators in the tracking mechanism - a high voltage controlled MEMS mirror (also known as Fast Steering Mirror, FSM) and a gimbal realized using two stepper motors with micro stepping.

After a successful acquisition of the transmitted laser beam, the A,B,C,D fiber cores are used for detection of beam deviation. Only the central fiber core is used for communication. In the test setup, the all five fiber cores are fed in the detection and amplification block, so that the received communication signal can be monitored ($U_{monitor}$). The four tracking cores signals ($U_{A,B,C,D}$) are then sampled by the APT system, and all further processing is done in the digital domain.

There are two tracking regulators running in simultaneously, one consist of PI regulation and is used for compensation of slow, but big changes in the beam position. The output of this regulation is sent with the frequency of 20Hz to stepper motor control modules using UART at the baudrate of 38400baud. The second tracking regulation is based on a PID regulation or an iterative tracking algorithm with adaptive step. This second tracking mechanism is used to compensate for fast changes of smaller magnitude. The result of the compensation is output at the rate of 1ksps by a 12bit DAC, boosted by a high voltage source and finally fed into the MEMS mirror internal electrodes which changes the tilt of the mirror in both X and Y axes.

The signals U_A, U_B, U_C and U_D can be defined by Equation 1. The constants C_1 and C_2 represent the gain of photodiode OTA circuit and logarithmic amplifier respectively. P_A is the optical power.

$$U_A = C_2 \cdot \log(C_1 \cdot P_A) \tag{1}$$

Based on the sampled voltages $U_{A,B,C,D}$, the position of the laser beam spot (x and y) is calculated using Equations 2 and 3 (as shown in [5]).

$$x = \frac{(U_B + U_C) - (U_A + U_D)}{U_A + U_B + U_C + U_D} \tag{2}$$

$$y = \frac{(U_A + U_B) - (U_C + U_D)}{U_A + U_B + U_C + U_D} \tag{3}$$

For each iteration, the error $e_{x,\ i}$ is calculated using Equation 4.

$$e_{x,\ i} = x_i - x_{i-1} \tag{4}$$

Based on the PID constants denoted as C_P, C_I and C_D and a chosen integration window constant N, the error signal Δ is calculated as per Equation 5.

$$\Delta = C_P \cdot e_{x,\ i} + C_I \cdot \sum_{j=i}^{i-N} e_{x,\ j} + C_D \cdot (e_{x,\ i} - e_{x,\ i-1}) \tag{5}$$

Finally, the calculated Δ is used to calculate next value of the voltage U_{hx} (Equation 6), setting the tilt of the FSM in the x axis. Similarly, the U_{hy} is calculated.

$$U_{hx,\ i} = U_{hx,\ i-1} + \Delta \tag{6}$$

In case the APT system detects that the receiving signal has been lost, the acquisition algorithm is restarted and the tracking is stopped by setting the FSM to the central position. The acquisition consists in scanning the Field of View (FoV) using the stepper motors until one of $U_{A,B,C,D}$ reaches a threshold. Then the tracking algorithm is restarted.

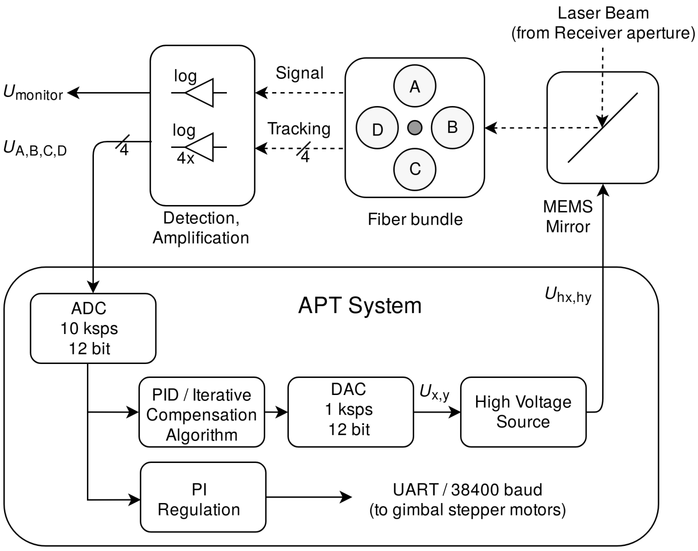

Fig. 1. Analyzed system principle of operation

III. APT Algorithm Analyzer

In order to verify the operation of PI, PID or iterative tracking algorithms an external hardware is needed to sample signals $U_{A,B,C,D}$, $U_{x,y}$ and $U_{monitor}$. Furthermore, the commands for the stepper motor controllers should also be monitored for a complete information about current state of the APT system.

Such analyzer device is shown in Figure 2. It consists of an analog front-end board with buffer amplifiers and 16bit, 1Msps ADCs. Those last are connected to the PRU co-processor and share the same clock signal. The serial interface implemented in software in the PRU allows for multiple Master In Slave Out (MISO) signals to be sampled at once. Thus a fully synchronous samples of input voltages is obtained. Those samples are then stored in the on board DDR memory in a circular buffer structure.

The main CPU (Cortex-A9) takes care of loading the firmware for the PRU and starts its sampling process. Then a dedicated Linux kernel module reads the circular buffer present in an on board DDR and stores the retrieved samples to the external USB Mass Storage Device (MSD).

In order to have a complete information about the state of the FSM - gimbal APT system, the commands sent to the gimbal stepper motor controllers via UART interface is also monitored. Since the used baud rate is only 38400baud, it is possible to sample this UART signal while sampling the high speed serial interface from ADCs (frequency of the CLK signal is 20MHz).

For storing the samples and the UART data to the circular buffer, a format with header is used in order to differentiate between them. A time stamp information is implicit and can be derived from the position of records containing the samples, which are stored at the frequency of 1MHz.

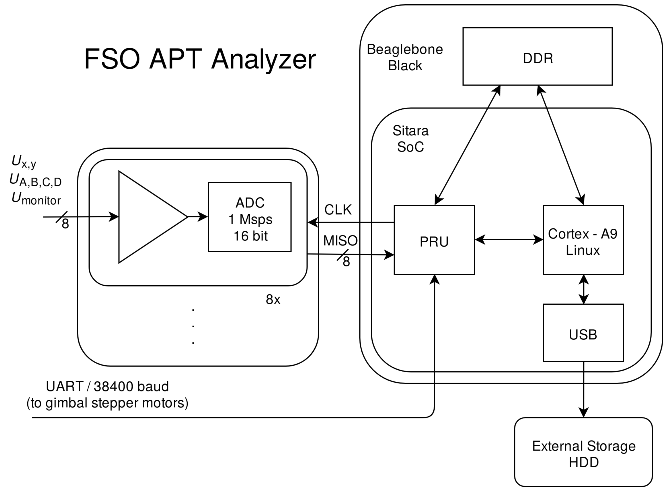

Fig. 2. Analyzer system

During the sampling process, no data interpretation is being done, this is left for the off-line post processing.

As the sampling frequencies of the APT system ADCs and DACs are two orders smaller than 1Msps, the record done by the APT analyzer should be sufficient for analysis of the APT algorithm and for reconstruction of the system state.

IV. APT System Parameters to Evaluate

The selection of P, I and D coefficients is done by using iterative algorithms and is not based on a formula, therefore following parameters can be measured after modification of each coefficient to learn how it affected the tracking system.

An iterative tracking algorithm is proposed in [4], which is an alternative to traditional PID regulator. The same approach will be used to compare its properties to the PID regulator.

A. *Response Time of FSM*

By using a mechanically stable laser beam source (in a laboratory), the response time of the MEMS FSM can be measured by observing the delay between a change of $U_{x,y}$ and $U_{A,B,C,D}$. This parameter is dependent on the mechanical properties of used FSM as well as on the analog signal conditioning chain (detection photodiode, band pass filter, logarithmic pre-amplifier). This delay limits the maximum frequency of the changes, which can be efficiently attenuated by the system.

B. *Stability of PID Regulator*

Low frequency mechanical vibrations (5-300Hz) are applied to the laser beam source fixture and the response signal at $U_{x,y}$ is observed. Harmonic signals are expected and their frequency (and phase) should correspond to the mechanical vibrations frequency (and phase).

C. Attenuation of Mechanical Vibrations

A residual harmonic signal is present at $U_{A,B,C,D}$ when the tracking algorithm is active. By comparing its amplitude before and after enabling the tracking algorithm, the attenuation at different frequencies is evaluated. The frequency range is limited by the properties of used FSM.

V. Conclusion

In this paper, a method of APT algorithm analysis was described and parameters to evaluate were announced. Thanks to the logging of APT system signals over time, it will be possible to verify the behavior of APT systems in real conditions. Future work will consist of using the developed analyzer to evaluate different APT algorithms or APT algorithms with different settings in order to optimize its performance.

Acknowledgment

The research described in this paper was financed by the Czech Ministry of Education in the frame of the National Sustainability Program under grant LO1401. For the research, the infrastructure of the SIX Center was used.

References

[1] M. A. Khalighi and M. Uysal, "Survey on Free Space Optical Communication: A Communication Theory Perspective," *IEEE Communications Surveys & Tutorials*, vol. 16, no. 4, pp. 2231–2258, 2014. [Online]. Available: http://ieeexplore.ieee.org/lpdocs/epic03/wrapper.htm?arnumber=6844864

[2] A. A. Farid and S. Hranilovic, "Outage Capacity Optimization for Free-Space Optical Links With Pointing Errors," *Journal of Lightwave Technology*, vol. 25, no. 7, pp. 1702–1710, jul 2007. [Online]. Available: http://ieeexplore.ieee.org/document/4267802/

[3] I. Ara, M. Mira, S. Fairooz, and A. Nazrul, "BER performance analysis of an optical M-ary PPM over FSO turbulent channel with pointing error using PIN receiver," in *2017 IEEE International Conference on Telecommunications and Photonics (ICTP)*. IEEE, dec 2017, pp. 242–246. [Online]. Available: http://ieeexplore.ieee.org/document/8285908/

[4] O. Barcik, P.; Novak, M.; Dobesch, A.; Kolka, Z.; Wilfert, "Concept of Fiber-Based Laser Beam Tracking System for Optical Wireless Communication," in *CSNDSP 2018*, Budapest, 2018, p. 4.

[5] V. Fernandez, J. Gomez-Garcia, A. Ocampos-Guillen, and A. Carrasco-Casado, "Correction of Wavefront Tilt Caused by Atmospheric Turbulence Using Quadrant Detectors for Enabling Fast Free-Space Quantum Communications in Daylight," *IEEE Access*, vol. 6, pp. 3336–3345, 2018. [Online]. Available: http://ieeexplore.ieee.org/document/8252707/

High dynamic range fluxgate magnetometer

David Novotný, Vojtěch Petrucha
Department of Measurement, Faculty of Electrical Engineering,
Czech Technical University in Prague

***Abstract*—In this paper, possibilities of achieving high dynamic range for fluxgate magnetometer are discussed. For a fluxgate sensor with its own noise in orders of few pT, operating in 60 uT Earth's magnetic field, dynamic range of >150 dB is necessary to exploit full potential of such a sensor. Even the most precise AD converters have usually maximum dynamic range of about 140 dB (given by its noise floor and full-scale range), so only digitization of the full sensor's output range isn't sufficient. In order to measure small variations in a large bias, a variometric arrangement can be used instead. ADC then digitizes only small range of the magnetometer as most of measured magnetic field is removed by a precise compensation system. This system must be very stable and low-noise as it has major impact on resulting noise and stability of the measurement. Low noise design based on precise analog components (AD, DA, voltage reference) controlled by FPGA with a soft-core processor is presented in this paper with a full characterization of the developed prototype.**

Keywords—fluxgate, FPGA, magnetometer, variometer

I. Introduction

Measurement of disturbances in Earth's magnetic field is important for many scientific and practical application such an earthquake detection and localization, Sun's activity measurement, geological prospecting, etc. [1,2]. These variations are very small, with magnitude in orders from tens of pT to few tens of nT in a frequency range approx. 1mHz-1Hz [2]. As a total value of Earth's magnetic field is around 50 µT (depending on location, 20-60 µT), high dynamic range of measurement is necessary. For this purpose, fluxgate sensors are preferred as they has lowest noise compared to other vector (room temperature operated) magnetometers [3]. Fluxgates are sometimes used in a combination with scalar type magnetometer [4] as this combination can benefit from their high long-term stability (and potentially can correct fluxgate drifts).

As one can found pretty hard to digitize signal with >150 dB dynamic range, another way is to remove "stable" part of measured signal instead and measure only small variations. Such concept is called variometer and requires very stable current source for driving compensation coils. Whole stability and noise of variometer is given by such a current source, and off course, by sensor itself.

One way is to use a constant current source for a stationary magnetometer, where bias field will be also static [5]. A prior knowledge is necessary to determine required current and coil constant leading to usability only in a small area of applications. Another option is to have controlled current source with at least few steps (only to get with measured value in ADC's range).

For this purpose, low noise, precise DAC AD5791B has been used. Its 20-bit resolution is unnecessary, but it has very good long term and temperature stability with a superior noise performance. With 167 nV_{RMS} noise in 0.1-10 Hz bandwidth and output span of 20 V, leads to noise floor of ~160 dB.

As DAC is in fact only a controllable voltage divider, stable and low noise voltage reference is a main part of the current source. It's parameters in a combination with DAC's parameters are determining resulting parameters of the whole circuit. State of the art bandgap reference LTC6655 has been used. It has 0.25 $ppm_{p\text{-}p}$ noise in the 0.1 to 10 Hz range [6], to get even lower with the noise, four LTCs has been placed in parallel to get half of a single reference's noise (which brings theoretically 155 dB limit).

For controlling whole variometer, FPGA has been used as it can implement all necessary logic, timing and even a soft-core microcontroller (Cortex M1).

II. Magnetometer design

A. Principle of operation

A magnetometer in a variometric arrangement usually incorporates a traditional analog fluxgate sensor that works only in a small range (e.g. ±3 µT) and output is held in approximately mid range (zero value) by variometric compensation system that has steps equal or smaller than half of fluxgate's range.

This compensation system can be done as dynamic (fluxgate is all the time controlled to not over-range) or "one-shot" when magnetometer's compensation is fixed (during installation at operation location) and after that doesn't change (potentially can get over-range, but high linearity and low signal distortion in that sub range is achieved).

Simplified diagram of the variometer operation can be seen in Fig. 1. Blue lines illustrates decreasing magnetic field, while red lines increasing. Hysteresis within half of ADC's range and equal to DAC step size can be seen.

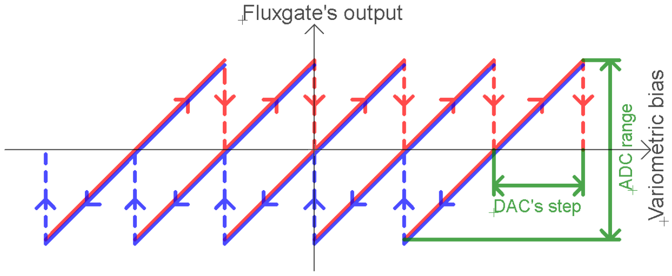

Fig. 1. Illustration of operation - dynamic ranging

B. Compensation system

As compensation current is always derived from the main voltage reference, it must be selected with high attention on noise and stability. Even state-of-the-art references aren't low-noise enough not to affect the measurement and the only way to lower their noise is using statistics (as their noise can be considered as uncorrelated, averaging output of N references lowers the noise by $\sqrt{N}$ factor).

Current through the compensation coils is controlled by a voltage to current converter (operational amplifier with a stable current sense resistor). Noise of such an amplifier and even the thermal noise of a sense resistor must be also taken into account.

Compensation coils are often tri-axial, compensating individual components of a magnetic field vector (in fluxgate's sensitivity directions).

C. *Fluxgate subsystem*

A traditional fluxgate circuit is used (processing of a second harmonic signal with an integrator feedback loop).

Sensor is kept in a precise zero magnetic field by feedback to maintain high linearity and stability, while variometric DAC keeps sensor only in approximately zero. Residuum compensated by fluxgate's feedback is digitized by ADC as measurement output (when summed with added variometric bias). Simple equation to combine DAC and fluxgate output is in (1).

$$B_{meas.} = C_{FG} \cdot U_{OUT\,FG} + C_{VAR} \cdot U_{OUT_{DAC}} \qquad (1)$$

Where $B_{meas.}$ *is measurement output [T],* C_{FG} *is fluxgate constant [V/T],* $U_{OUT\,FG}$ *is fluxgate's output voltage,* C_{VAR} *variometric compensation's contant [T/V] and* $U_{OUT_{DAC}}$ *is output voltage of DA converter [V].*

D. *FPGA controller*

For fluxgate excitation and synchronous demodulator control, FPGA can be used with the advantage of logic reprogramability. It is typically necessary to tune phase shift between excitation and demodulator signals which is easy to implement in the FPGA. Some of them also allows to use IP-core microprocessors such as Cortex-M1, designed for FPGAs or 8051-like cores [7].

III. PRACTICAL REALIZATION

A simplified block diagram of designed magnetometer can be seen in Fig 3. Fig 2 is a photograph of a complete magnetometer setup with all necessary supporting electronics.

Fig. 2. Photograph of complete magnetometer with sensor head in right corner

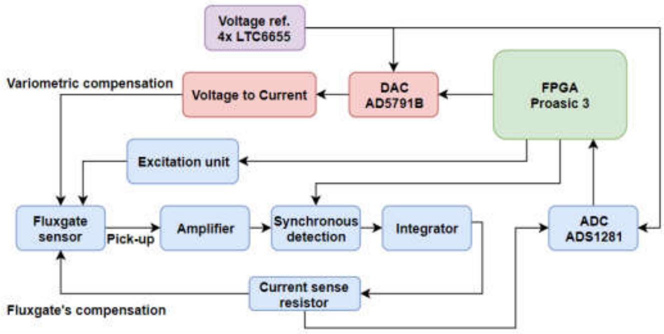

Fig. 3. Simplified block diagram of the instrument

A. *Voltage reference circuit*

To lower the drift of voltage references (LTC6655), four of them have been connected to average their outputs. Measured noise can be compared to theoretical $\sqrt{N}$ decay in Fig. 4.

With 5 V nominal voltage, specified 0.25 $ppm_{p\text{-}p}$ noise in 0.1 to 10 Hz band should equal to 1.25 $\mu_{p\text{-}p}$ and approx. 190 nV_{RMS}. It can be seen that such a value hasn't been achieved even through careful low-noise design (measured with a spectrum analyzer and very-low-noise preamp based on LT1028).

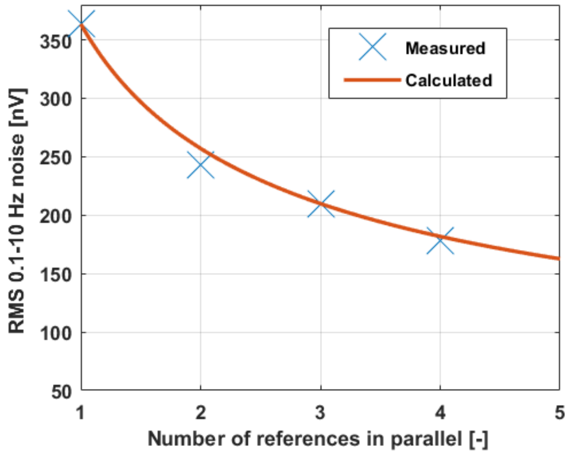

Fig. 4. Measured and calculated noise of multiple LTC6655

B. ***Digital to Analog converter***

AD5791B has been used as a currently available lowest noise and most stable DA converter. Noise measurement has been done with using only one and then with all four references. Initial noise of DAC, rising proportionally to output voltage can be seen in Fig. 5.

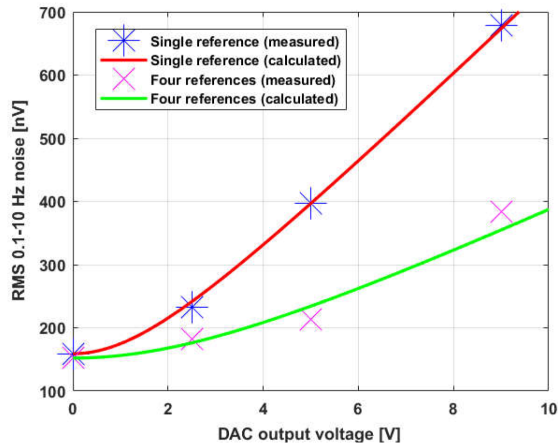

Fig. 5. Measured and modeled noise of DAC vs. output voltage

Dependence of noise on output voltage can be modeled as in (2), when noise is considered as uncorrelated.

$$U_{n_{TOTAL}} = \sqrt{U_{n_{DAC}}^2 + \left(U_{n_{REF}} \cdot \frac{U_{OUT}}{U_{REF_{NOM}}}\right)^2} \qquad (2)$$

With $U_{n_{DAC}}$ [VRMS] intrinsic noise of DAC, nominal reference voltage $U_{REF_{NOM}}$[V], noise of references $U_{n_{REF}}$ [VRMS] and output voltage of DAC U_{OUT} [V].

With measurement in Fig. 5. DAC's intrinsic noise of 160 nV_{RMS} can be found. This value can be compared to 1.1 $\mu V_{p\text{-}p}$ catalogue value [9] which is approx. equal to 167 nV_{RMS}. This measurement also leads to noise description of the whole magnetometer in dependence on measured field as in Fig. 6.

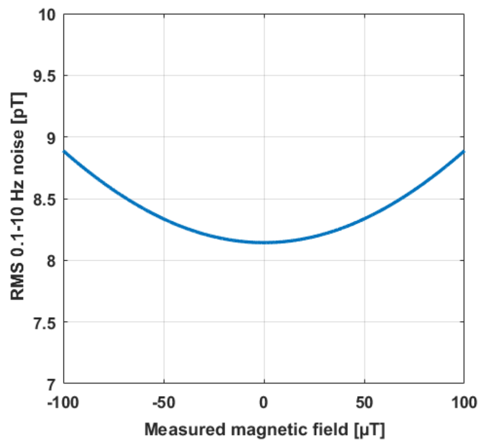

Fig. 6. Simulated noise dependence on measured magnetic field

C. *Summing of compensation's*

While most of measured magnetic field is compensated by variometric compensation, small residuum is still compensated by analog fluxgate's compensation. Summing of this two compensations can be done with two individual coils with separate voltage to current converters or with one converter and summing resistors node. Two coils design has been used and tested. Desired compensation constant's ratio is tuned with turn counts of used Merritt coils [8] and by current sense resistors.

D. *Magnetometer model*

For stability and step response verification, a Matlab Simulink model has been created. Small signal (without DAC bias change) and large signal step response (dynamic variometer mode) can be seen in Fig. 7 and Fig. 8. Fluxgate with its feedback (small-signal response) can be modeled as a LTI system with transfer function given by (3).

$$H(s) = \frac{U_{out}}{B_{meas.}} = \frac{\frac{R_S}{K_C}}{\frac{\tau\cdot(R_C+R_S)}{K_C\cdot G_d\cdot C_S}\cdot s+1} \qquad (3)$$

Where U_{out} is output voltage [V], $B_{meas.}$ is measured magnetic field [T], R_s is resistance of current sense resistor [Ω], R_c resistance of feedback coil [Ω], τ time constant of an integrator [s], K_c coil constant [T/A], G_d gain of preamplifier [V/V], C_s open-loop sensitivity of fluxgate [V/T].

Time constant τ_s of a feedback compensation is given by (4) with real parameters of magnetometer and resulting low-pass cut-off frequency f_C by (5).

$$\tau_s = \frac{\tau\cdot(R_C+R_S)}{K_C\cdot G_d\cdot C_S} \cong \frac{1}{115{,}2} \cong 8.7\ ms \qquad (4)$$

$$f_C = \frac{1}{2\cdot\pi\cdot\tau_s} \cong 18.3\ Hz \qquad (5)$$

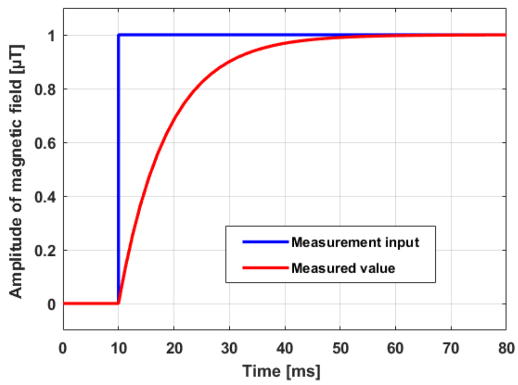

Fig. 7. Small signal step response of variometer

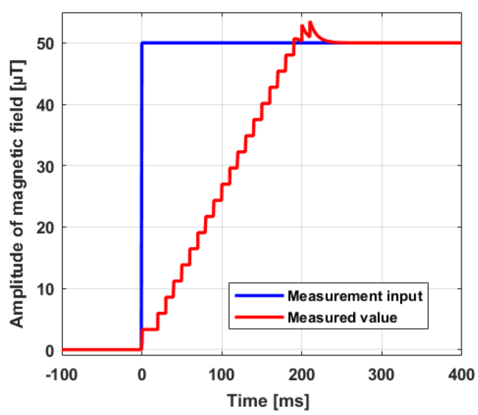

Fig. 8. Large signal step response of variometer (dynamic mode)

IV. MEASURED PARAMETERS OF THE MAGNETOMETER

A. *Noise characterization*

Firstly, sensor's intrinsic noise has been measured. Sensor head with a ring-core fluxgate has been placed into 6-layer Permalloy shielding, operated in open-loop, processed with

SR830 lock-in amplifier. In Fig. 9, measured noise spectral density can be seen with a typical 1/f character and marker placed at 1 Hz, showing amplitude of 2.08 $pT/\sqrt{Hz}$ and integral noise has been 8 pT_{RMS} (0.1-10 Hz).

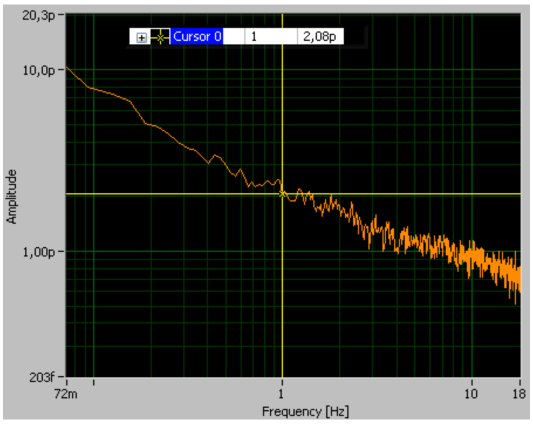

Fig. 9. Noise density spectrum of open loop fluxgate sensor

For a complete magnetometer working in a closed loop, total noise has been measured and can be found as approx. 18 pT_{RMS} and with noise density of 4.5 $pT/\sqrt{Hz}$ at 1 Hz (Fig. 10). A bit worse result in a comparison to open-loop measurement with lock-in amplifier is given by fluxgate's demodulator noise as disconnection of variometric feedback haven't noticeable effect on noise.

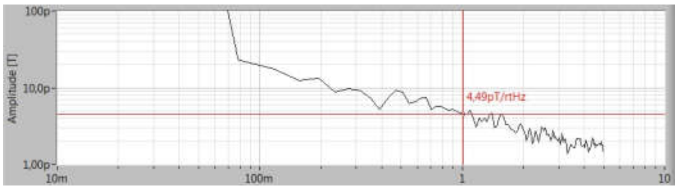

Fig. 10. Noise density spectrum of designed magnetometer

B. *Variometer's linearity in full range*

With correctly calibrated ratio between fluxgate's and variometric compensations, linearity error as small as in Fig. 11 has been measured (two separate measurements, red and blue line). Linearity error can be found as small as ±10 ppm in ±100 µT range.

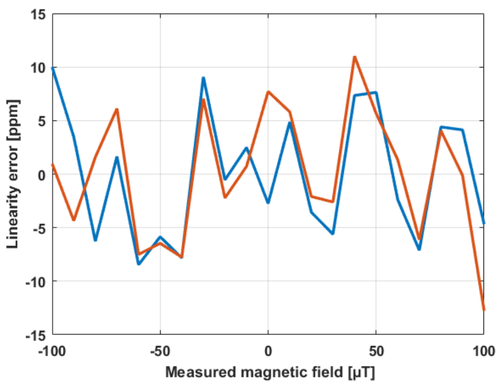

Fig. 11. Linearity error measurement

V. CONCLUSIONS

With the presented variometric method, desired dynamic range has been almost reached, with approx. 18 pT_{RMS} noise within ±100 µT range of measurement, noise floor is -141 dB. Reduction of fluxgate's electronics noise is still under progress, targeting to reach open-loop noise measured with a lock-in amplifier. Theoretically maximum limit given only by used fluxgate sensor is 8 pT_{RMS} (-148 dB), when measured and modeled noise of variometric compensation is taken into account, 9 pT_{RMS} (-147 dB) noise floor should be achieved.

When power consumption, price and dimensions of magnetometer's electronics aren't much important, LTZ1000A can be considered as LTC6655 replacement, as it has even lower noise (but requires moderate amount of supporting electronics and has not negligible power consumption as it is thermo-stated buried Zener diode).

Linearity of a presented variometer is reaching values typical for single-range "full-field" magnetometers and makes it very precise and versatile.

ACKNOWLEDGMENT

This work was supported by the Student Grant Competition (SGS) at CTU in Prague, No. SGS18/081/OHK3/1T/13.

REFERENCES

[1] J. Valenta, “Introduction to Geophysics: Lecture Notes”, available at: http://www.geology.cz/ (7/2018).

[2] S. M. Potirakis, A. Schekotov, T. Asano, and M. Hayakawa, “Natural time analysis on the ultra-low frequency magnetic field variations prior to the 2016 Kumamoto (Japan) earthquakes”, *Journal of Asian Earth Sciences*, vol. 154, pp. 419-427, 2018.

[3] P. Ripka, "Magnetic Sensors and Magnetometers," Artech House, 2001

[4] L. Tøffner-Clausen, V. Lesur, N. Olsen, and C. C. Finlay, “In-flight scalar calibration and characterisation of the Swarm magnetometry package”, *Earth, Planets and Space*, vol. 68, no. 1, p. -, 2016.

[5] M. Janošek, V. Lesur, M. Vlk, and C. C. Finlay, “Low-noise magnetic observatory variometer with race-track sensors”, *IOP Conference Series: Materials Science and Engineering*, vol. 108, no. 1, p. 012026-, Mar. 2016.

[6] Linear Technology (Analog Devices), "LTC6655 datasheet", available at: https://www.analog.com/ (7/2018)

[7] Microsemi, "FPGA IP Cores", available at: https://www.microsemi.com/ (7/2018)

[8] J. L. Kirschvink, “Uniform magnetic fields and double-wrapped coil systems: Improved techniques for the design of bioelectromagnetic experiments, ” Bioelectromagnetics, vol. 13.5, pp. 401-411, 1992.

[9] Analog Devices, "AD5791 datasheet", available at: https://www.analog.com/ (7/2018)

On Ultrasonic Gas Leak Detector Testing Methods

Petr Skryja, Marek Novak
Department of Radio Electronics
Faculty of Electrical Engineering and Communication
Brno University of Technology
Technicka 12
616 00 Brno (Czech Republic)
Email: xskryj01@vutbr.cz, xnovak0m@vutbr.cz

***Abstract*—This paper deals with a simulation of gas leak for a purpose of testing ultrasonic gas leak detectors. Principle of a sound creation and major techniques of the detection are described. Three methods suitable for simulation of the gas leak are analytically introduced. Commercially sold detectors and methods for testing are presented.**

I. Introduction

In many industries, high-risk substances, particularly flammable and toxic ones are used and manufactured. There are occasional gas leaks that generate financial losses, potential hazards for industrial companies, their employees and people living in the neighborhood. To reduce these risks, it is crucial to use devices such as gas detectors. These can help provide more time to take corrective or protective measures. In development, it is necessary to test the detector to verify its proper functionality during normal firmware and hardware changes. [1]

II. Ultrasonic Gas Leak Detector (UGLD)

Ultrasonic gas detection uses an acoustic sensor to identify noise fluctuations that are imperceptible to human ear. If the gas moves from a high pressure zone through a hole to a low pressure region, "hissing" is generated. This " hissing " is a broad band noise, ranging in frequency from Hz to tens of MHz. From this frequency range, it is clear that part of the sound lies in an audible area and part in an ultrasonic area. A level depends on the pressure drop accros the leak (P_1 and P_2), a physical size of the leak (S) and the gas properties (M) as shown in Figure 1. [2]

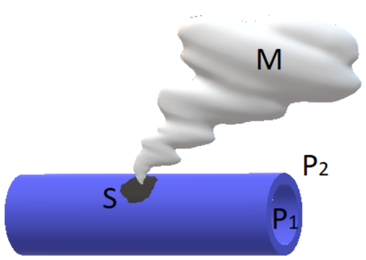

Fig. 1. Gas leakage

Figure 2 shows a blue curve which represents an ordinary spectrum without gas leakage. It can be seen that there is a lot of noise in the audible band, unlike the ultrasonic band. For this reason, only the ultrasonic band is used to detect gas leakage. [3] A green and a red curves show two different gas leaks. It can be seen that the spectrum grows significantly above the noise and a higher frequencies are more attenuated.

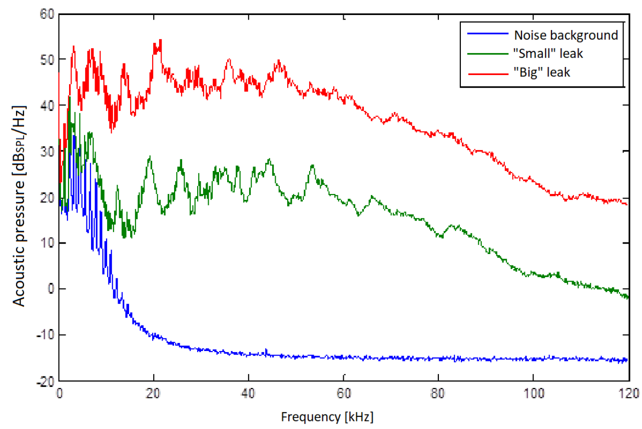

Fig. 2. Spectrum generated by gas leakage [4]

A dependence of a spectrum attenuation on a distance from a source is shown in Figure 3. Higher frequencies are again more attenuated.

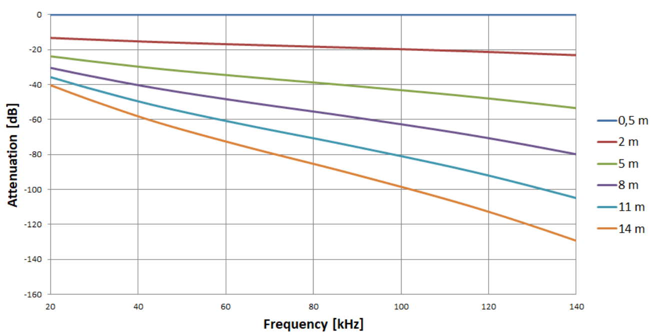

Fig. 3. Attenuation of generated sound over in ultrasonic frequency band

On a market there are several types of these detectors using different methods of processing signals from the microphone. For example, a microprocessor, an FPGA, or even a neural network is used. The detectors use a piezoelectric microphone to capture sound, and milliampere loop (4-20mA), RS-485, and several relays to communicate with the outside world. Using these means, it is possible to determine a status of alarms, whether the detector is functional or to read a data.

III. Testing Methods

There are three major techniques for testing the correct leakage detection. In all cases, there is a control system in a circuit that controls the leakage simulation and evaluates a correct detection. The correct detection is compared by connecting the control system to the milliampere loop, relays or RS-485 of UGLD.

A. Test method using an electronically controllable valve

Figure 4 shows the first option to generate leakage using compressed air and an electronically controlled valve, through which air escapes thereby creating ultrasound. This method makes it possible to simulate the real ultrasonic spectrum of a gas leakage. The disadvantage may be more complicated realization and the impossibility of realizing other spectrums.

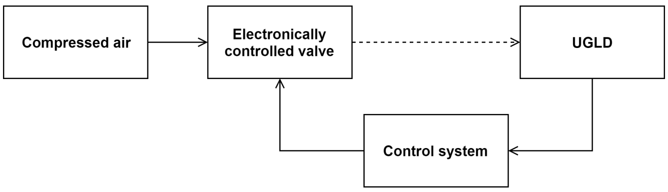

Fig. 4. Test method using an electronically controllable valve

B. Test method using ultrasonic microphone

Another option is to use an ultrasonic speaker as it is shown in figure 5. The speaker has sensitivity characteristics shown in figure 6. This characteristic has a maximum at the frequency of 40 kHz, so the speaker is tuned to one frequency. It follows that before generating the sound (for example using a computer) it is necessary to calculate this curve and adjust the resulting signal accordingly. This method offers a relatively simple implementation that can generate different signals / spectrums, which can perform more complex detector tests. However, when testing, it is necessary to calculate the distance of the speaker from the detector according the Figure 3.

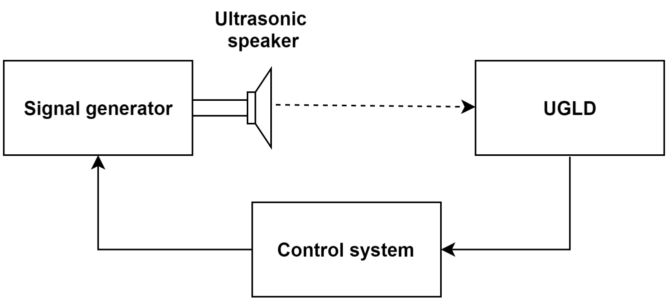

Fig. 5. Test method using ultrasonic microphone

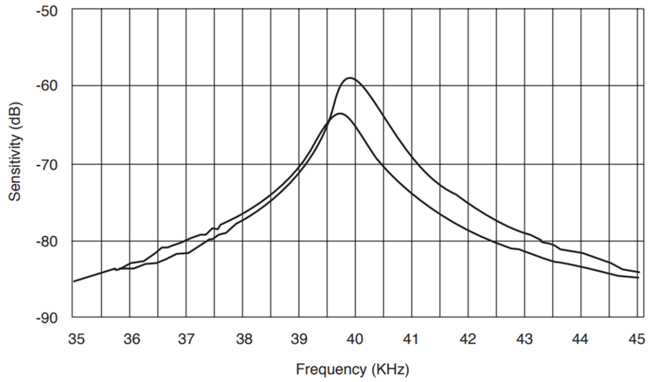

Fig. 6. Sensitivity characteristic of ultrasonic speaker [5]

C. Test method using a signal generator connected instead of the piezoelectric sensor detector

The last option is to replace the sensor with a signal generator (see Figure 7). This intervention will affect the test as the detector will not be tested as a whole. Even this method makes it possible to generate different spectra, but must be calculated with the sensitivity characteristic of acoustic sensor of the detector. An advantage can be in the direct connection of the signal generator and the detector, where it is not necessary to calculate the distance between the signal source and the sensor.

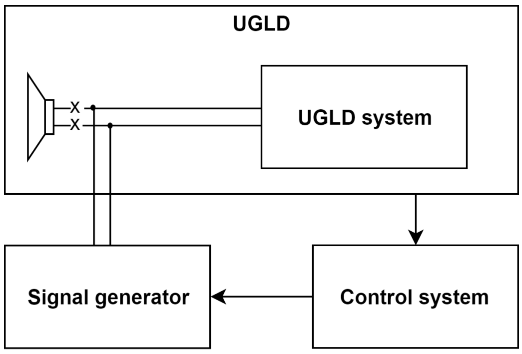

Fig. 7. Test method using a signal generator connected instead of the piezoelectric sensor detector

IV. Converting the Voltage from the Piezoelectric Sensor to the Sound Pressure Level (SPL)

To calculate the sound pressure level in dB is first necessary to convert the voltage to acoustic pressure in units of Pa, which is performed by Equation 1

$$U_{RMS}[Pa] = \frac{U_{RMS}}{C_{microphone}} \tag{1}$$

where U_{RMS} is voltage level of a sample [mV] and $C_{microphone}$ is microphone sensitivity constant [mV/Pa].

$$SPL[dB] = 20 \cdot log_{10}(\frac{U_{RMS}[Pa]}{P_{ref}}) \tag{2}$$

where P_{ref} is reference the pressure of 20 μPa.

V. Conclusion

In this paper, a behavior of the gas leakage spectrum was introduced and a three major techniques for testing the correct leakage detection was described. Thanks to this test, it is possible to make changes in the detector, which is performed in its development and test its proper functioning. Future work will consist of modeling a spectrum characteristic of gas leaks, compressor compression, and other sounds that may appear near these detectors.

Acknowledgment

The research described in this paper was financed by the Czech Ministry of Education in the frame of the National Sustainability Program under grant LO1401. For the research, the infrastructure of the SIX Center was used.

References

[1] Honeywell, *GasBook*. Honeywell Analytics, 2013. [Online]. Available: https://www.honeywellanalytics.com/ /media/honeywell-analytics/documents/english/11296_gas-book_v5_0413_lr_en.pdf?la=en-gb

[2] Gassonic, “ULTRASONIC GAS LEAK DETECTION TECHNOLOGY.” [Online]. Available: http://www.gassonic.com/technology/the_technology/

[3] Emerson, “About Ultrasonic Gas Leak Detectors,” 2017. [Online]. Available: http://www.emerson.com/en-us/automation/measurement-instrumentation/flame-gas-detection/about-ultrasonic-gas-leak-detectors

[4] P. Skryja, *Automatické testování detektoru úniku plynu*. Vysoké učení technické v Brně, Fakulta elektrotechniky a komunikačních technologií, Ústav radioelektroniky, 2018, no. Diplomova prace.

[5] Kobitone, “Ultrasonic Transducers,” 2007. [Online]. Available: https://cz.mouser.com/datasheet/2/209/KT-400288-1171943.pdf

A high directional low profile lens antenna for a 77 GHz car radar

Jaroslav ZECHMEISTER
Faculty of Electrical Engineering and Communication
Brno University of Technology
Brno, Czech Republic
xzechm02@stud.feec.vutbr.cz

***Abstract*—This paper focuses on a high directional low profile lens antenna for a car radar. The antenna is designed for 77 GHz band. Its total height is 40 mm and has gain more than 27 dBi. For the lens fabrication, different 3D printing technologies and materials are used and compared.**

***Keywords*—car radar; lens antenna; dielectric lens; 3D printing;**

I. Introduction

The important goal of automotive engineering is safety and comfort of passengers, which in recent years allows to increase the rapidly development of car systems. These systems can be divided to active and passive [1]. For example, a passive comfort system is parking assistance, which warning a driver of obstacles. An adaptive cruise control is one of the active comfort systems. It in dependence on a situation in front of the car controls the speed during driving. The adaptive cruise control is closely linked to emergency brake system, which in danger of accident stops the car. It can be considered as the active safety system. An example of the passive safety systems is blind spot detection of the rear-view mirrors [1].

For those systems, the developing of car sensors scanning a vehicle surround is important. Nowadays, the development of the car radar is very increasing. Its depending to improvement of microwave integrated circuits, which comes be more available. The defined frequency bands for telematics are
24 GHz and 77 GHz [1]. The 24 GHz band is primarily used for near-range car radars with wide angular width. In this frequency band, planar antennas are preferable. In 77 GHz range high directivity antennas are typically used for long range car radar with high angular resolution, like lens antennas, antenna arrays etc.

II. Lens antenna design

A. Dielectric lens design

Dielectric lenses are applied to horn antennas to enhancement directivity. For good parameters of proposed lens antenna, the focal point of lens should be in the same place as phase center of the horn antenna.

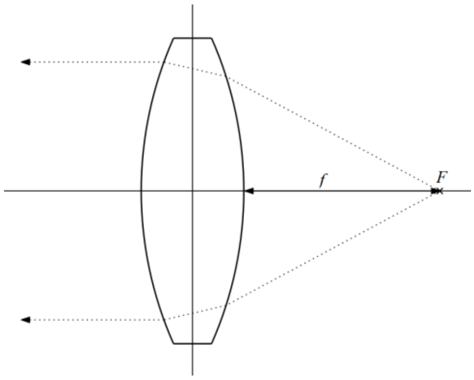

Figure 1. Spherical lens model.

Spherical lens (Figure 1) is composed of two curved surfaces. If the radii are same, the focal length *f* can be obtained by (1)

$$f = \frac{nr^2}{\left(2\left(r-\sqrt{r^2-R^2}+d_0\right)(n-1)^2\right.} \qquad (1)$$

where ε_r is relative permittivity of dielectric material, *r* is radius of curvatures, *R* is radius of lens and d_0 is thickness on peripheral of the lens.

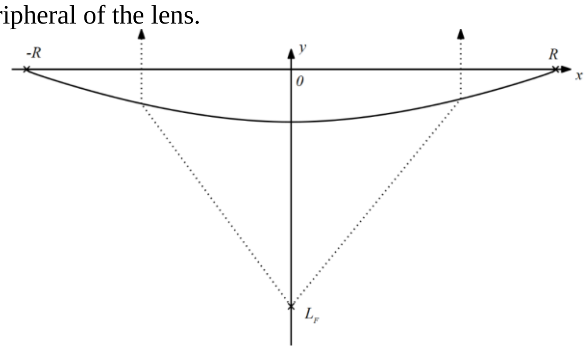

Figure 2. Hyperbolic lens model.

Hyperbolic lens (Figure 2) can be classified like aspherical lens. The shape of curvature of the hyperbolic lens is described by (2).

$$y = \frac{-\left(\sqrt{\varepsilon_r(R^2+f^2)}-L_F\right)+\sqrt{\left(\sqrt{\varepsilon_r(R^2+f^2)}-f\right)^2-(\varepsilon_r-1)(R^2-x^2)}}{\varepsilon_r-1} \quad (2)$$

where ε_r is relative permittivity, f is focal length, R is radius of lens and x is distance of center of the lens.

B. Dielectric lens comparison

For the comparison of influence of the proposed spherical and hyperbolical lenses to the antenna parameters, they were placed to aperture of conventional horn antenna designed by using nomograms considering the low profile of antenna [2]. The horn antenna was fed by WR12 waveguide. The phase center of horn antenna was determined by using CST Microwave Studio. Distance of the phase center from the aperture was 39,05 mm, and both lenses were designed with relative permittivity 2.5. The comparison of antenna gain between conventional horn antenna and lens antenna with both types of lenses is shown in Figure 3.

The influence of the lens to the antenna parameters is almost identical. In this case only geometrical parameters of the lenses can be considered for the next using. The hyperbolic lens has an advantage in the geometric aspect, as it does not interfere beyond the aperture of the antenna.

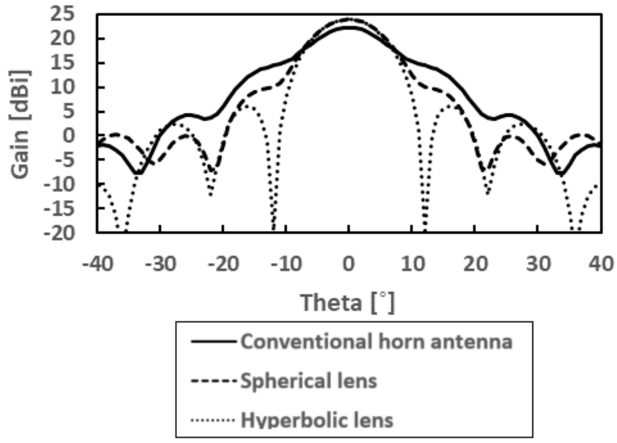

Figure 3. The comparison of antenna gain between conventional horn antenna and lens antennas.

C. Influence of relative permittivity

The enhancement of gain is achieved by increasing the radius of the aperture. The radius can be enlarged to the point where radiation energy begins to flow into the side lobes. At this point, maximum gain can be obtained. The ideal radius is different for various relative permittivity of lens materials. The dependence of the ideal radius on the relative permittivity of the lens material is shown in Figure 4. The dependence is almost linear. The gain obtained by the ideal radii is shown in Figure 5. As seen, the characteristic in 4.5 starts be less steep. Therefor is advantageous choose the permittivity between 3.5 - 4.5 with consider to the maximal gain and geometrical aspects of the final antenna. The ideal radius was simulated with respect to the 40 mm antenna profile.

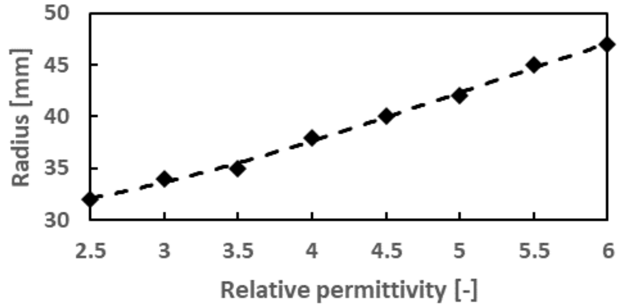

Figure 4. The dependence of ideal radius on relative permittivity of lens material.

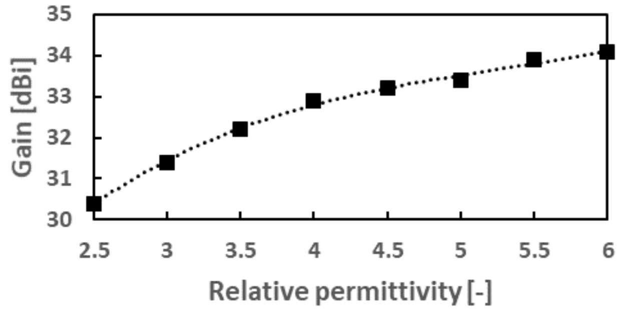

Figure 5. The dependence of maximal gain on relative permittivity of lens material.

III. EXPERIMENTAL RESULTS

A. Fabrication of lenses

The dielectric lenses were fabricated by 3D printing technologies as fused deposition modelling and stereolithography. Both lenses had a radius 33 mm, which is less than the ideal radius, and different optimized focal length. The lens of acrylonitrile butadiene styrene (ABS) was fabricated by fused deposition modelling. This method consists in the layering of the melted material to the final structure. The individual layers are visible on the final structure (Figure 6A). The measured relative permittivity of ABS was 2.42 and the optimized focal length was 39.5 mm.

The second lens was fabricated by the stereolithography 3D printing technology. This method uses photopolymerization to fashion the final structure. The photopolymer resin is hardened with an ultraviolet laser. The final structure fabricated by this method is almost perfectly smooth (Figure 6B). The used photopolymer had relative permittivity 2.8. The optimized focal length of the proposed lens was 38.4 mm.

The lens antenna consisted of lenses and manufactured brass horn. The horn had aperture radius of 33 mm, same as the lenses, and a 40 mm profile. The horn was chemically silvered for a better surface conductivity (Figure 6C).

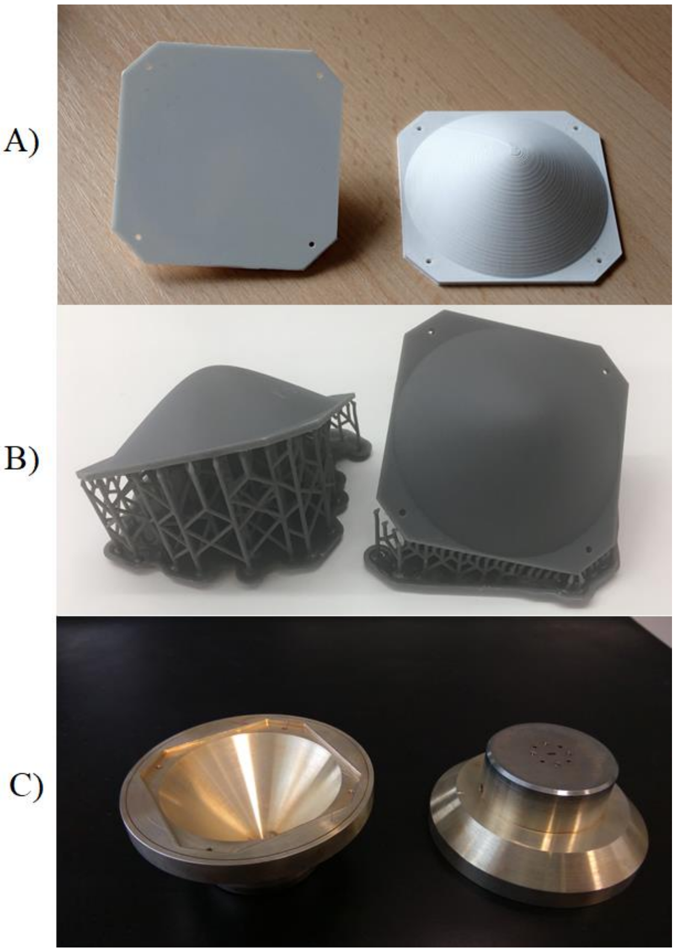

Figure 6. The fabricated lens of ABS (A) and photopolymer (B) and horn antenna (C).

B. Comparison between measurement and simulated data

Figure 7 shows the comparison between simulated and measured gain at 77 GHz of the lens antenna with the ABS lens. The simulated antenna gave 27.7 dBi and the fabricated antenna 27.9 dBi. The simulated angular width of the main lobe was 4.1˚ in E-plane and 6.5˚ in H-plane. The measured values were 3.8˚ in E-plane and 5.5˚ in H-plane. The simulated and measured results of reflection frequency characteristics for the antenna are shown in Figure 8. The antenna achieved a sufficient wide bandwidth for impedance matching where the reflection coefficients were below -10 dB.

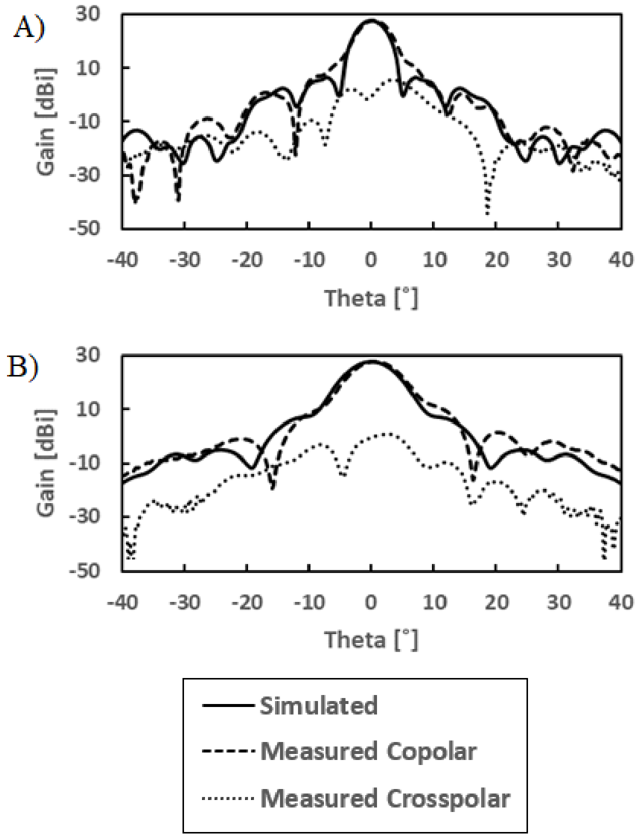

Figure 7. The comparison between simulated and measured gain of the lens antenna with the ABS lens in E-plane (A) and H-plane (B).

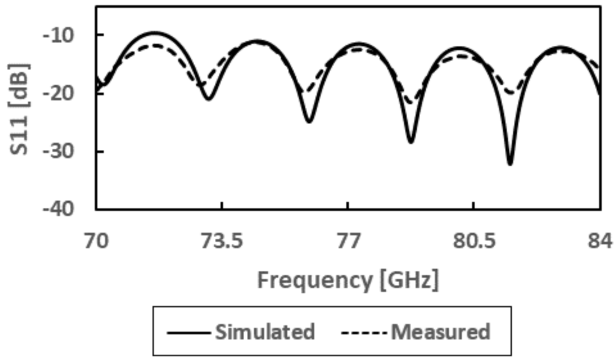

Figure 8. The comparison between simulated and measured reflection coefficient of the lens antenna with the ABS lens.

The simulated and measured gain at 77 GHz of the lens antenna with the photopolymer lens is shown in Figure 9. The maximum gain of the simulated antenna was 27 dBi and the fabricated antenna was 27.6 dBi. The angular width of main lobe in H-plane was 5.7˚ for simulation and 4.5˚ for measurement respectively. Figure 10 shows simulated and measured results of the reflection coefficient frequency response for the lens antenna with photopolymer lens. The impedance matching bandwidth for the reflection coefficients less -10 dB is wider than 14 GHz.

The simulated and measured parameters of the antennas are summarized in Table 1.

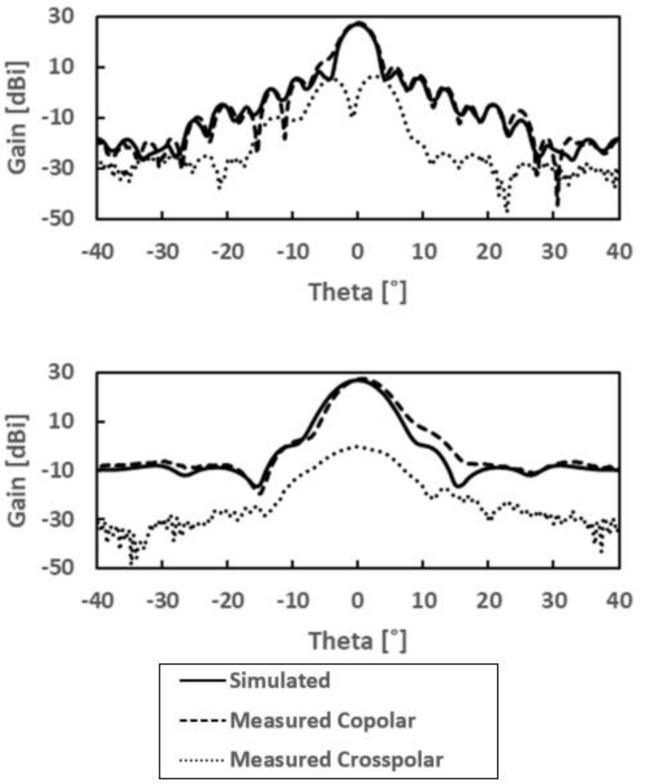

Figure 9. The comparison between simulated and measured gain of the lens antenna with the photopolymer lens in E-plane (A) and H-plane (B).

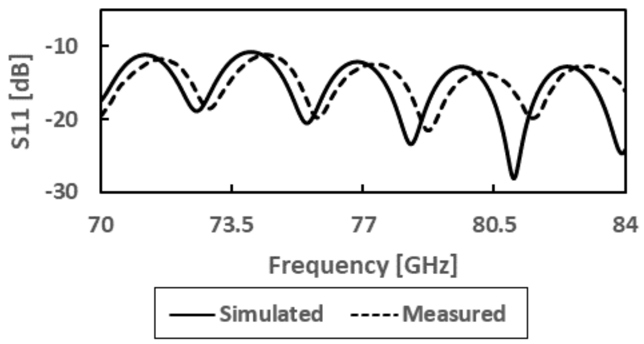

Figure 10. The comparison between simulated and measured reflection coefficient of the lens antenna with the photopolymer lens.

	Simulated			Measured		
Material of lens	**G[dBi]**	**Θ_E[°]**	**Θ_H[°]**	**G[dBi]**	**Θ_E[°]**	**Θ_H[°]**
ABS	27.7	4.1	6.5	27.9	3.8	5.5
Photopolymer	27	3.5	5.7	27.6	3.8	4.5

Table 1. The comparison between simulated and measured parameters of lens antennas made from different material of lenses

IV. CONCLUSION

A high directional lens antenna with 40 mm low profile for a 77 GHz car radar with 3D printed lenses is presented. The influence of the material relative permittivity of the lens to antenna parameters is described. Simulated antennas provided good estimation to the fabricated antennas. The fabricated lens antenna with an ABS lens achieved gain of 27.9 dBi and 3 dB beamwidth of 3.8° in E-plane and 5.5° in H-plane. The side lobe level of gain was 21 dB below the main lobe. The lens antenna with photopolymer lens gave 27.6 dBi maximal gain. The 3 dB beamwidth in the E-plane and H-plane were 3.8° and 4.5°, respectively. The antenna gave a side lobe level less than 19 dB.

ACKNOWLEDGMENT *(HEADING 5)*

The author would like to thank Zbynek Lukes for many helpful comments, valuable discussion and also for fabrication of the ABS lens. Further thanks to Jaroslav Lacik for carrying out material measurements and article revision. Last but not least, thanks to Ramet a.s. for horn antenna fabrication and support.

REFERENCES

[1] HASCH, J., TOPAK, E., SCHNABEL, R., ZWICK, T., WEIGEL, R., WALDSCHMIDT, Ch. Millimeter-Wave Technology for Automotive Radar Sensors in the 77 GHz Frequency Band. IEEE Transactions on Microwave Theory and Techniques [online]. 2012, 60(3), 845-860.

[2] BALANIS, A.C. Antenna Theory: Analysis and Design, 2/E. New York: J. Wiley & Sons, 1996.

[3] ZECHMEISTER, J. Anténní systém pro automobilový radar. Brno: Vysoké učení technické v Brně, Fakulta elektrotechniky a komunikačních technologií, 2018. 79 s. Vedoucí diplomové práce doc. Ing. Jaroslav Láčík, Ph.D..